

Hybrid-Field Joint Channel and Visible Region Estimation for RIS-Assisted Communications

Xiaokun Tuo, *Graduate Student Member, IEEE*, Ming-Min Zhao, *Senior Member, IEEE*, Xiang Wang, Changsheng You, *Member, IEEE*, and Min-Jian Zhao, *Member, IEEE*

arXiv:2602.06313v1 [eess.SP] 6 Feb 2026

Abstract—In reconfigurable intelligent surface (RIS)-assisted millimeter-wave (mmWave) communication systems, the large-scale RIS introduces pronounced geometric effects that lead to the coexistence of far-field and near-field propagation. Furthermore, random blockages induce spatial non-stationarity across the RIS array, causing signals from different scatterers to illuminate only partial regions, referred to as visible regions (VRs). This renders conventional far-field and fully visible array-based channel models inadequate and makes channel estimation particularly challenging. In this paper, we investigate the non-stationary cascaded channel estimation problem in a hybrid-field propagation environment, where the RIS-base station (BS) link operates in the far-field, while the user-RIS link exhibits near-field characteristics with partial visibility. To address the resulting high-dimensional and coupled estimation problem, a reduced-dimensional sparse bilinear representation is developed by exploiting the structural characteristics of the cascaded channel. In particular, a dictionary compression technique is proposed to represent the high-dimensional coupled dictionary using a low-dimensional polar-domain dictionary weighted by a visibility matrix, thereby significantly reducing the problem scale. Based on this representation, a turbo-structured joint Bayesian estimation (TS-JBE) approach is proposed to simultaneously estimate the channel gains, VRs, and off-grid parameters, thereby avoiding error propagation inherent in existing sequential methods. Simulation results demonstrate that the proposed method significantly improves the estimation accuracy compared with existing approaches.

Index Terms—reconfigurable intelligent surface, hybrid-field, channel estimation, visible region, Bayesian estimation.

I. INTRODUCTION

WITH the rapid increase in the number of mobile devices and the proliferation of wireless applications, future wireless networks are facing unprecedented challenges in terms of peak data rate, spectral efficiency, energy efficiency, and reliability [1], [2]. As a promising candidate for sixth-generation (6G) communications, reconfigurable intelligent surfaces (RISs) have recently attracted significant attention due to the capability of reconfiguring wireless propagation environment in a cost-effective and energy-efficient manner

X. Tuo, M. M. Zhao and M. J. Zhao are with the College of Information Science and Electronic Engineering, Zhejiang University, Hangzhou 310027, China and also with the Zhejiang Provincial Key Laboratory of Multi-Modal Communication Networks and Intelligent Information Processing, Hangzhou 310027, China (e-mail: xktuo@zju.edu.cn; zmmblack@zju.edu.cn; mjzhao@zju.edu.cn).

X. Wang is with the School of Information and Navigation, Air Force Engineering University, Xi'an 710077, China (e-mail: lleafwx626@126.com).

C. You is with the Department of Electronic and Electrical Engineering, Southern University of Science and Technology (SUSTech), Shenzhen 518055, China (e-mail: youcs@sustech.edu.cn).

[3], [4]. A RIS typically consists of a large number of nearly passive reflecting elements whose reflection coefficients can be programmed to manipulate the phase of incident electromagnetic waves [3], [4]. Through appropriate configuration of these elements, RISs can provide additional degrees of freedom to enhance signal coverage, suppress interference, and improve both spectral and energy efficiency. Owing to their low hardware cost, negligible power consumption, and ease of deployment, RISs can be densely integrated into existing wireless infrastructures, making them particularly attractive for large-scale and high-frequency 6G scenarios.

The performance gains of RIS-assisted systems, however, critically rely on the availability of accurate channel state information (CSI). Unlike conventional active antenna arrays, RIS elements are passive and incapable of signal reception or baseband processing, which makes CSI acquisition particularly challenging [5]. Moreover, RIS usually comprises a large number of reflecting elements, causing the dimension of RIS-associated cascaded channels to scale rapidly with the array size. Although on-off reflection schemes have been proposed to decouple the cascaded channels by selectively activating RIS elements during the training phase, thereby enabling the use of conventional channel estimation methods [6], such approaches still incur excessive training overhead and high computational complexity. To address these challenges, extensive research efforts have been devoted to channel estimation in RIS-assisted communication systems. To enable channel estimation with all RIS elements simultaneously activated, methods based on conventional estimators, such as least-squares (LS) [7], [8] and linear minimum mean-square error (LMMSE) [9], have been proposed under properly designed training protocols. In addition, compressed sensing (CS)-based approaches exploit the sparsity of cascaded channels to reduce pilot overhead, including improved orthogonal matching pursuit (OMP) algorithms [10], [11]. Moreover, matrix factorization-based methods further leverage the sparsity and low-rank properties of cascaded channels for efficient channel estimation [12], [13].

It is worth noting that the aforementioned works are developed under far-field planar-wave assumptions. However, to meet the stringent performance requirements of 6G systems, RISs are expected to be deployed with a large physical aperture and operate at millimeter-wave (mmWave) or even terahertz frequencies. As a consequence, the Rayleigh distance increases significantly, and users or scatterers are often located in the near-field region of the RIS. In such scenarios, the conventional planar-wave model becomes inaccurate, and spherical-

wave propagation needs to be incorporated for accurate channel modeling and estimation. Unlike the angular-domain sparsity exhibited under the planar-wave assumption, channels modeled with spherical-wave propagation exhibit inherent sparsity in the polar domain. To effectively capture this property for near-field channel estimation, [14] proposed a novel polar-domain grid construction scheme, enabling a sparse representation of near-field channels in the polar domain. Building upon the spherical-wave propagation model, recent studies have explored near-field channel estimation for RIS-assisted systems. Stage-wise approaches have been developed to progressively recover the angular- and polar-domain parameters of the cascaded channel, reducing training overhead [15]. Beyond this, unified hybrid-field channel models have been proposed for extremely large intelligent reflecting surface (XL-IRS)-assisted orthogonal frequency division multiplexing (OFDM) systems, where tensor-based OMP combined with variational Bayesian inference (VBI) was employed to jointly estimate and track the channel [16]. In addition, [17] considered a double-RIS-assisted mmWave communication scenario, adopted a spherical-wave-based near-field channel model, and proposed a cascaded channel modeling and analysis approach to characterize near-field propagation effects and evaluate system performance.

Beyond near-field propagation, the enlargement of RIS arrays inevitably introduces spatial non-stationarity [18]. Specifically, due to geometric effects and random blockages, signals associated with different scatterers illuminate only partial regions of the RIS, which are referred to as visible regions (VRs). Ignoring spatial non-stationarity leads to severe model mismatch and performance degradation, especially for large-aperture RIS deployments. To tackle this issue, several studies have investigated joint VR detection and channel estimation for RIS-assisted communication systems. For instance, [19] studied joint near-field localization and channel reconstruction in XL-RIS-assisted systems. However, this work mainly considered the line-of-sight (LoS) path between the RIS and the user, while neglecting non-line-of-sight (NLoS) multipath components, which limits its applicability in practical environments. In [20], a hybrid channel model was introduced, together with the concept of VRs in RIS systems, and a two-stage algorithm was proposed to perform joint channel estimation and VR detection. Nevertheless, the inherent error propagation caused by the two-stage processing remains unavoidable and degrades the overall estimation performance.

Motivated by the above observations, this paper investigates the cascaded channel estimation problem in RIS-assisted communication systems. We propose a joint Bayesian estimation approach that enables simultaneous inference of cascaded sparse channel gains, VRs, and off-grid parameters. The main contributions of this paper are summarized as follows:

- A hybrid-field cascaded channel model is developed for RIS-assisted mmWave systems, where the RIS-base station (BS) channel is modeled in the far-field, while the user-BS channel is characterized by near-field propagation with explicit VR modeling to capture spatial non-stationarity.
- By exploiting structural characteristics of the cascaded

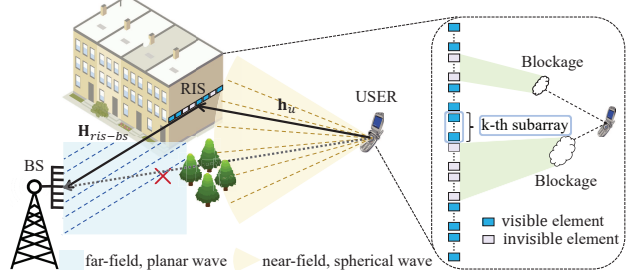


Fig. 1: Considered RIS-aided mmWave system model.

channel, a compression strategy for high-dimensional coupled dictionaries is introduced to construct a reduced-dimensional sparse bilinear channel representation, thereby significantly reducing the problem scale and effectively alleviating the resulting multi-dimensional, strongly coupled estimation problem.

- Based on the proposed channel representation, a turbo-structured joint Bayesian estimation (TS-JBE) approach is developed to jointly estimate the cascaded sparse channel gains, VRs, and off-grid parameters, thereby avoiding the error propagation inherent in conventional stage-wise estimation schemes.
- Simulation results demonstrate that the proposed approach achieves superior normalized mean squared error (NMSE) performance compared with existing approaches, validating its effectiveness under hybrid-field and spatially non-stationary propagation conditions.

The rest of this paper is organized as follows. Section II introduces the system model. Section III presents the sparse representation of the cascaded channel and the hierarchical sparse prior model. Section IV elaborates on the proposed TS-JBE algorithm. Section V presents numerical results to validate the effectiveness of the proposed approach. Finally, Section VI concludes the paper.

Notations: Scalars, vectors and matrices are respectively denoted by lower/upper case, boldface lowercase and boldface uppercase letters. The transpose, conjugate, and conjugate transpose of a general vector \mathbf{z} are denoted by \mathbf{z}^T , \mathbf{z}^* , and \mathbf{z}^H , respectively. The operators $\|\cdot\|$, and $|\cdot|$ denote ℓ_2 -norm, and absolute value, respectively. The notation $\langle f(z) \rangle_{q(z)} = \int f(z)q(z) dz$ denotes the expectation of $f(z)$ with respect to the random variable z distributed according to $q(z)$. $\text{diag}(\mathbf{z})$ denotes a diagonal matrix with diagonal \mathbf{z} , and $\text{vec}(\mathbf{Z})$ stacks the columns of \mathbf{Z} into a vector. Its inverse operator $\text{unvec}_{r \times c}(\cdot)$ reshapes a vector of length rc into an $r \times c$ matrix in a column-wise manner. $\Re(\cdot)$ and $\Im(\cdot)$ denote the real and imaginary parts, respectively. \odot , \otimes , $*$, and \bullet denote the Hadamard product, Kronecker product, row-wise Khatri-Rao product, and column-wise Khatri-Rao product, respectively. \mathbb{R} and \mathbb{C} denote the sets of real and complex numbers. $\mathcal{CN}(\mathbf{z}; \boldsymbol{\mu}, \boldsymbol{\Sigma})$ denotes the complex Gaussian distribution with mean $\boldsymbol{\mu}$ and covariance $\boldsymbol{\Sigma}$, and $\Gamma(z; a, b)$ denotes the Gamma distribution with shape parameter a and rate parameter b .

II. SYSTEM MODEL

As illustrated in Fig. 1, consider a RIS-aided multiple-input multiple-output (MIMO) system operating in the mmWave band under the time-division duplex (TDD) mode. The BS is equipped with M antennas, while the RIS comprises N reflecting elements, satisfying $N \gg M$. The RIS is partitioned into K subarrays, each consisting of N/K reflecting elements. Within each subarray, all elements are assumed to share identical visibility, since the channel can be regarded as spatially stationary over a small aperture [21]. A single-antenna user is served, with the RIS deployed in its vicinity to enhance the communication performance.¹ Both the BS and RIS employ uniform linear arrays (ULAs) with half-wavelength spacing, i.e., $d = \lambda/2$. The direct user-BS link is assumed to be blocked by obstacles (e.g., trees or buildings), so that communication relies solely on the cascaded user-RIS and RIS-BS channels, with $\mathbf{h}_u \in \mathbb{C}^{N \times 1}$ and $\mathbf{H} \in \mathbb{C}^{M \times N}$ denoting the corresponding channel gains, respectively.

A. Channel Model

In conventional array modeling, targets located in the far-field region are typically characterized using the planar-wave assumption. The array response vector (ARV) of an N -element ULA is then $\mathbf{a}^f(\varphi) = [1, e^{-j\frac{2\pi}{\lambda}d\varphi}, \dots, e^{-j\frac{2\pi}{\lambda}(N-1)d\varphi}]^T$, where d is the inter-element spacing, λ is the carrier wavelength, and $\varphi = \cos\phi$ is the spatial angle corresponding to the physical angle of arrival (AoA) or departure (AoD). When the target enters the near-field region, the planar-wave model is no longer valid, and a spherical-wave assumption is required to characterize the wavefront curvature [1]. Accordingly, the near-field ARV can be expressed as $\mathbf{a}^n(\vartheta, r) = [e^{-j\frac{2\pi}{\lambda}(r^{(1)}(\vartheta, r) - r)}, \dots, e^{-j\frac{2\pi}{\lambda}(r^{(N)}(\vartheta, r) - r)}]^T$, where $\vartheta = \cos\theta$ denotes the spatial angle, r denotes the distance from the reference element to the target, and $r^{(n)}(\vartheta, r)$ denotes the distance between the n -th array element and the target, which is uniquely determined by (ϑ, r) and the array geometry. The near- and far-field regions are separated by the Rayleigh distance $Z = \frac{2(D_r^2 + D_s^2)}{\lambda}$, where D_r and D_s denote the receive and transmit array apertures [1]. In mmWave RIS-aided MIMO systems, the large number of antennas or reflecting elements results in an enlarged physical aperture. Since the RIS is typically deployed in close proximity to the user, the user-RIS distance is often comparable to or even smaller than the Rayleigh distance. Consequently, the user-RIS link operates in the near-field region and should be modeled using a spherical-wave propagation assumption [22]. Accordingly, the user-RIS and RIS-BS links are modeled using spherical-wave and planar-wave propagation, respectively. Without loss of generality, we consider a Cartesian coordinate system in which the RIS is placed along the x -axis, with its leftmost element located at the origin, i.e., $\mathbf{n} = [0, 0]^T$. The BS array is positioned along the y -axis, and the topmost BS element

¹The proposed approach can be extended to the multiuser scenario by allowing each user to transmit orthogonal pilot sequences, thereby enabling the separation and estimation of the cascaded channels for each user.

is located at $\mathbf{m} = [x_{BS}, y_{BS}]^T$.² Based on this geometric configuration, the cascaded channel can be modeled as follows.

1) *User-RIS Channel*: For the l -th propagation path between the user and RIS, where $l \in \mathcal{L}_U \triangleq \{1, \dots, L_U\}$ and L_U denotes the number of user-related paths ($l = 1$ corresponding to the LoS path from the user), the position of the corresponding scatterer (or the user) is given by $\mathbf{r}_{U,l} = [r_{U,l} \cos \theta_{U,l}, r_{U,l} \sin \theta_{U,l}]^T$, where $\theta_{U,l}$ denotes the physical AoA of the l -th path, and $r_{U,l}$ represents the reference distance from the RIS array to the corresponding scatterer (or the user). In particular, $\mathbf{r}_{U,1} = \mathbf{u}$ corresponds to the user location. Accordingly, the distance between the n -th RIS element and the l -th scatterer (or the user) is given by $r_{U,l}^{(n)} = \|\mathbf{r}_{U,l} - \mathbf{n}_n\|$, where $\mathbf{n}_n = [(n-1)d, 0]^T$ denotes the position vector of the n -th RIS element. Based on the spherical-wave propagation model, the near-field ARV associated with the l -th path is defined as $\mathbf{a}(\vartheta_{U,l}, r_{U,l}) = [e^{-j\frac{2\pi}{\lambda}(r_{U,l}^{(1)} - r_{U,l})}, \dots, e^{-j\frac{2\pi}{\lambda}(r_{U,l}^{(N)} - r_{U,l})}]^T$, where $\vartheta_{U,l} = \cos \theta_{U,l}$ denotes the corresponding spatial angle. Using the Fresnel approximation [23], the distance $r_{U,l}^{(n)}$ can be approximated as

$$r_{U,l}^{(n)} \approx r_{U,l} - (n-1)d\vartheta_{U,l} + \frac{d^2(n-1)^2(1-\vartheta_{U,l}^2)}{2r_{U,l}}. \quad (1)$$

Furthermore, a binary indicator vector is usually employed to capture the non-stationary characteristics of the channel [19], [24], [25]. We introduce $\phi_l \in \{0, 1\}^{N \times 1}$ to indicate the visibility of RIS elements for the l -th propagation path. Specifically, the n -th entry of ϕ_l is equal to 1 if the n -th RIS element is visible to the l -th path, and 0 otherwise. With this definition, the user-RIS channel can be modeled as

$$\mathbf{h}_u = \sum_{l=1}^{L_U} \alpha_l \mathbf{a}(\vartheta_{U,l}, r_{U,l}) \odot \phi_l, \quad (2)$$

where α_l denotes the complex-valued path gain of the l -th path.

2) *RIS-BS Channel*: For the BS-RIS MIMO channel, each path is characterized by an AoA at the BS and an AoD at the RIS. Specifically, the AoA and AoD of the l -th path are denoted by $\vartheta_{B,l} = \cos \theta_{B,l}$ and $\varphi_{R,l} = \cos \phi_{R,l}$, respectively, where $l \in \mathcal{L}_{RB} \triangleq \{1, \dots, L_{RB}\}$ and L_{RB} denotes the total number of propagation paths between the RIS and BS. Accordingly, the RIS-BS channel can be expressed as

$$\mathbf{H} = \sum_{l=1}^{L_{RB}} \beta_l \mathbf{a}_B(\vartheta_{B,l}) \mathbf{a}_R^H(\varphi_{R,l}), \quad (3)$$

where β_l denotes the complex-valued gain of the l -th path.

3) *Hybrid-field Cascaded Channel*: The effective channel from the user to the BS via the RIS is determined by the RIS-BS channel \mathbf{H} , the user-RIS channel \mathbf{h}_u , and the configurable phase shifts applied at the RIS. Specifically, the n -th RIS element imposes a phase shift $\nu_n \in [0, 2\pi)$ on the reflected signal, which corresponds to a reflection coefficient $\eta_n = e^{j\nu_n}$. Collecting all reflection coefficients yields the phase-shift

²Although a 2D coordinate system is considered here for simplicity, the proposed method can be directly extended to a 3D coordinate system by appropriately modifying the array response dictionaries.

vector $\boldsymbol{\eta} = [\eta_1, \eta_2, \dots, \eta_N]^T$, and the associated diagonal phase-shift matrix is given by $\boldsymbol{\Theta} = \text{diag}(\boldsymbol{\eta})$. Accordingly, the hybrid-field cascaded channel can be expressed as

$$\mathbf{h} = \mathbf{H} \boldsymbol{\Theta} \mathbf{h}_u. \quad (4)$$

During uplink training, the user transmits P pilot symbols with transmit power P_t . After pilot correlation and normalization, the resulting equivalent observation is given by

$$\mathbf{y}_p = \mathbf{H} \boldsymbol{\Theta}_p \mathbf{h}_u + \mathbf{n}_p = \mathbf{h}_p + \mathbf{n}_p, \mathbf{n}_p \sim \mathcal{CN}(\mathbf{0}, \frac{\sigma^2}{P_t} \mathbf{I}_M), \quad (5)$$

where $\mathbf{h}_p \triangleq \mathbf{H} \boldsymbol{\Theta}_p \mathbf{h}_u$ denotes the effective cascaded channel associated with the p -th pilot and σ^2 denotes the noise variance. Stacking the signals over all pilot intervals yields

$$\tilde{\mathbf{y}} = [\mathbf{y}_1^T, \dots, \mathbf{y}_P^T]^T = \tilde{\mathbf{h}} + \tilde{\mathbf{n}}, \quad (6)$$

where $\tilde{\mathbf{h}} = [\mathbf{h}_1^T, \dots, \mathbf{h}_P^T]^T$ and $\tilde{\mathbf{n}} = [\mathbf{n}_1^T, \dots, \mathbf{n}_P^T]^T$.

III. SPARSE CHANNEL REPRESENTATION AND PRIOR MODELING

In this section, a sparse representation of the cascaded channel is developed, and the associated prior models are introduced by exploiting the structural characteristics of the RIS-aided hybrid-field propagation environment. Specifically, a generic pilot transmission indexed by p is considered. For notational convenience, the pilot index p is omitted whenever no ambiguity arises. Accordingly, the received signal, the corresponding effective cascaded channel, and the noise are denoted by \mathbf{y} , \mathbf{h} , and \mathbf{n} , respectively, each corresponding to a specific portion of $\tilde{\mathbf{y}}$, $\tilde{\mathbf{h}}$ and $\tilde{\mathbf{n}}$ indexed by p .

A. Sparse Representation and Model Transformation

1) *Sparse Representation*: To exploit the inherent sparsity of the cascaded channel, a grid-based sparse representation is adopted. Two uniform angular grids are defined for the BS and RIS as $\boldsymbol{\vartheta} \triangleq [\vartheta_1, \dots, \vartheta_M]^T$ and $\boldsymbol{\varphi} \triangleq [\varphi_1, \dots, \varphi_N]^T$ with M and N points, respectively. The grid points are given by $\vartheta_m = \frac{2}{M} \left(m - \frac{M+1}{2} \right)$ for $m \in \mathcal{M} \triangleq \{1, \dots, M\}$, and $\varphi_n = \frac{2}{N} \left(n - \frac{N+1}{2} \right)$ for $n \in \mathcal{N} \triangleq \{1, \dots, N\}$. Let $\mathbf{a}_B(\vartheta_m) \in \mathbb{C}^{M \times 1}$ and $\mathbf{a}_R(\varphi_n) \in \mathbb{C}^{N \times 1}$ denote the far-field ARVs at the BS and RIS for the corresponding grid points. Stacking these ARVs yields the far-field array response dictionaries $\mathbf{F}_M \in \mathbb{C}^{M \times M}$ and $\mathbf{F}_N \in \mathbb{C}^{N \times N}$. Accordingly, the RIS-BS channel admits the sparse representation $\mathbf{H} = \mathbf{F}_M \mathbf{A} \mathbf{F}_N^H$, where $\mathbf{A} \in \mathbb{C}^{M \times N}$ is a sparse gain matrix and the superscript (\circ) denotes the ideal on-grid case.

Moreover, the spatial sparsity of the near-field user-RIS channel is more naturally characterized in the polar domain. We construct a non-uniform polar-domain grid $[\boldsymbol{\vartheta}_u, \mathbf{r}_u] \triangleq [\vartheta_1, r_1; \dots; \vartheta_{\bar{N}}, r_{\bar{N}}]$, where $\bar{N} = N_p S$, and N_p and S denote the numbers of angular and radial samples, respectively, following the discretization rule in [14]. Let $\mathbf{a}(\vartheta_{\bar{n}}, r_{\bar{n}}) \in \mathbb{C}^{N \times 1}$ denote the near-field ARV at the \bar{n} -th grid point, and stack them to form the polar-domain dictionary $\mathbf{W} \in \mathbb{C}^{N \times \bar{N}}$. The user-RIS channel is then expressed as $\mathbf{h}_u = (\mathbf{W} \odot \boldsymbol{\Phi}) \mathbf{b}$, where

$\boldsymbol{\Phi}$ is a binary VR matrix and \mathbf{b} is a sparse vector of complex-valued gains. Specifically, each nonzero b_l of \mathbf{b} corresponds to the l -th propagation path with visibility indicated by ϕ_l , the l -th column of $\boldsymbol{\Phi}$, as in (2). Based on the above representations, the overall hybrid-field cascaded channel can be rewritten as

$$\overset{\circ}{\mathbf{h}} = \mathbf{F}_M \mathbf{A} \mathbf{F}_N^H \text{diag}(\boldsymbol{\eta})(\mathbf{W} \odot \boldsymbol{\Phi}) \mathbf{b}, \quad (7)$$

2) *Model Transformation*: From the cascaded channel model in (7), the unknown parameters are identified as the far-field sparse gain matrix \mathbf{A} , the VR matrix $\boldsymbol{\Phi}$, and the near-field sparse gain vector \mathbf{b} . These parameters jointly characterize the cascaded channel via a multi-linear coupling relationship. To facilitate efficient parameter inference, some fundamental matrix identities are exploited to reformulate (7). Specifically, by appropriately rearranging the cascaded channel expression, the received signal can be expressed in equivalent linear forms with respect to either the VR matrix $\boldsymbol{\Phi}$ or the vectorized cascaded sparse gain $\text{vec}(\mathbf{b}^T \otimes \mathbf{A})$, while treating the remaining parameters as known. Mathematically, by defining $\bar{\mathbf{W}} = \mathbf{W} \odot \boldsymbol{\Phi}$, we have

$$\begin{aligned} \overset{\circ}{\mathbf{h}} &= \mathbf{F}_M \mathbf{A} \mathbf{F}_N^H \text{diag}(\boldsymbol{\eta})(\bar{\mathbf{W}} \mathbf{b}) \\ &= \mathbf{F}_M \mathbf{A} \mathbf{F}_N^H \text{diag}(\bar{\mathbf{W}} \mathbf{b}) \boldsymbol{\eta} \\ &\stackrel{(a)}{=} (\boldsymbol{\eta}^T \otimes \mathbf{I}_M) \text{vec}(\mathbf{F}_M \mathbf{A} \mathbf{F}_N^H \text{diag}(\bar{\mathbf{W}} \mathbf{b})) \\ &\stackrel{(b)}{=} (\boldsymbol{\eta}^T \otimes \mathbf{I}_M) \text{vec}(\mathbf{F}_M (\mathbf{b}^T \bar{\mathbf{W}}^T \bullet \mathbf{A} \mathbf{F}_N^H)) \\ &\stackrel{(c)}{=} (\boldsymbol{\eta}^T \otimes \mathbf{I}_M) \text{vec}(\mathbf{F}_M (\mathbf{b}^T \otimes \mathbf{A}) (\bar{\mathbf{W}}^T \bullet \mathbf{F}_N^H)) \\ &\stackrel{(d)}{=} (\boldsymbol{\eta}^T \otimes \mathbf{I}_M) ((\bar{\mathbf{W}}^T \bullet \mathbf{F}_N^H)^T \otimes \mathbf{F}_M) \text{vec}(\mathbf{b}^T \otimes \mathbf{A}) \\ &\stackrel{(e)}{=} (\boldsymbol{\eta}^T \otimes \mathbf{I}_M) ((\bar{\mathbf{W}} * \mathbf{F}_N^*) \otimes \mathbf{F}_M) \text{vec}(\mathbf{b}^T \otimes \mathbf{A}), \end{aligned} \quad (8)$$

where (a) and (d) follow from the vectorization identity, i.e., $\text{vec}(\mathbf{ABC}) = (\mathbf{C}^T \otimes \mathbf{A}) \text{vec}(\mathbf{B})$, (b) holds from the property of diagonal matrices and the Khatri-Rao product, i.e., $\mathbf{X} \text{diag}(\mathbf{v}) = \mathbf{v}^T \bullet \mathbf{X}$, (c) follows from the property of the Khatri-Rao product, i.e., $(\mathbf{A} \otimes \mathbf{B})(\mathbf{C} \bullet \mathbf{D}) = (\mathbf{AC}) \bullet (\mathbf{BD})$, and (e) follows from the row-wise and column-wise Khatri-Rao products relation, i.e., $\mathbf{A} * \mathbf{B} = (\mathbf{A}^T \bullet \mathbf{B}^T)^T$ [26].

Directly estimating the cascaded sparse channel gain vector $\text{vec}(\mathbf{b}^T \otimes \mathbf{A}) \in \mathbb{C}^{\bar{N}N \times 1}$ results in a prohibitively large problem size due to the direct coupling between the near-field and far-field dictionaries, rendering practical channel estimation computationally infeasible. Therefore, it is essential to exploit the structural characteristics of the cascaded channel model in (8) to reduce the dimension of the estimation problem and, consequently, the computational burden. In particular, the coupled hybrid-field dictionary term $\bar{\mathbf{W}} * \mathbf{F}_N^*$ in (8), arising from the interaction between the near-field and far-field dictionaries at the RIS, introduces potential column redundancy and is the primary source of the dimension expansion. If this coupled dictionary can be efficiently compressed, the overall problem dimension can be substantially reduced. Existing studies have shown that the inner product between a near-field ARV and a dimension-compatible far-field ARV can be equivalently represented by a new near-field ARV [20]. This equivalence compresses the representation of the coupled dictionary from a high-dimensional angular-radial parameterization to a compact

angle-distance pair. Building on this insight, Proposition 1 further demonstrates that the row-wise Khatri-Rao product of the near-field and far-field dictionaries can be equivalently represented by a low-dimensional near-field dictionary when the near-field ARV is coupled with the VR indicator vector.

Proposition 1. The row-wise Khatri-Rao product between the near-field dictionary considering VR indicator $\bar{\mathbf{W}}$ and the conjugate of the far-field dictionary \mathbf{F}_N^* , i.e., $\bar{\mathbf{W}} * \mathbf{F}_N^*$ is equivalent to the Hadamard product between a near-field dictionary $\mathbf{Q} \in \mathbb{C}^{N \times \bar{Q}}$ with grid $[\bar{\varphi}, \bar{r}] \in \mathbb{R}^{\bar{Q} \times 2}$ and a VR matrix $\bar{\Phi} \in \{0, 1\}^{\bar{N} \times \bar{Q}}$:

$$\bar{\mathbf{W}} * \mathbf{F}_N^* \Leftrightarrow \mathbf{Q} \odot \bar{\Phi}, \quad (9)$$

where \Leftrightarrow denotes that the cascaded channel \mathbf{h} preserves the same number of active columns under the transformation between the two dictionaries $\bar{\mathbf{W}} * \mathbf{F}_N^*$ and $\mathbf{Q} \odot \bar{\Phi}$.

Proof. Please refer to Appendix A. \square

Based on Proposition 1, \mathbf{h} can be rewritten as

$$\begin{aligned} \mathbf{h} &= (\boldsymbol{\eta}^T \otimes \mathbf{I}_M)((\bar{\mathbf{W}} * \mathbf{F}_N^*) \otimes \mathbf{F}_M) \text{vec}(\mathbf{b}^T \otimes \mathbf{A}) \\ &= (\boldsymbol{\eta}^T \otimes \mathbf{I}_M)((\mathbf{Q} \odot \bar{\Phi}) \otimes \mathbf{F}_M) \text{vec}(\mathbf{X}), \end{aligned} \quad (10)$$

where $\mathbf{X} \in \mathbb{C}^{M \times \bar{Q}}$ denotes the joint sparse matrix associated with the transformed dictionary $(\mathbf{Q} \odot \bar{\Phi}) \otimes \mathbf{F}_M$. It is worth noting that the above dictionary transformation also alters the indexing of the sparse representation. As a result, $\text{vec}(\mathbf{X})$ is generally not identical to $\text{vec}(\mathbf{b}^T \otimes \mathbf{A})$, while both representations uniquely characterize the same cascaded channel. Moreover, the proposed transformation substantially reduces the representation dimension. Specifically, the sparse vector describing the cascaded channel is reduced from $\text{vec}(\mathbf{b}^T \otimes \mathbf{A}) \in \mathbb{C}^{MN\bar{N} \times 1}$ to $\text{vec}(\mathbf{X}) \in \mathbb{C}^{M\bar{Q} \times 1}$, leading to a reduction in representation scale from $\mathcal{O}(MN^2)$ to $\mathcal{O}(MN)$, since \bar{Q} is comparable to N , as both result from the same near-field grid generation algorithm applied to the same array. This dimension reduction significantly alleviates the dictionary size and results in a substantial decrease in computational complexity. Building upon the reduced-dimensional representation \mathbf{X} , the cascaded channel can be vectorized as

$$\mathbf{h} = \mathbf{D}_1(\bar{\Phi}) \mathbf{x}, \quad (11)$$

where $\mathbf{x} \triangleq \text{vec}(\mathbf{X})$ and $\mathbf{D}_1(\bar{\Phi}) = (\boldsymbol{\eta}^T \otimes \mathbf{I}_M)((\mathbf{Q} \odot \bar{\Phi}) \otimes \mathbf{F}_M)$. This indicates that \mathbf{h} admits a linear representation with respect to the cascaded sparse channel gain vector \mathbf{x} .

Furthermore, (10) can be equivalently reformulated as

$$\begin{aligned} \mathbf{h} &= (\boldsymbol{\eta}^T \otimes \mathbf{I}_M)((\mathbf{Q} \odot \bar{\Phi}) \otimes \mathbf{F}_M) \mathbf{x} \\ &\stackrel{(f)}{=} (\mathbf{x}^T \otimes (\boldsymbol{\eta}^T \otimes \mathbf{I}_M)) \text{vec}((\mathbf{Q} \odot \bar{\Phi}) \otimes \mathbf{F}_M) \\ &\stackrel{(g)}{=} (\mathbf{x}^T \otimes (\boldsymbol{\eta}^T \otimes \mathbf{I}_M)) \text{vec}((\mathbf{Q} \otimes \mathbf{F}_M) \odot (\bar{\Phi} \otimes \mathbf{1}_{M \times M})) \\ &\stackrel{(h)}{=} (\mathbf{x}^T \otimes (\boldsymbol{\eta}^T \otimes \mathbf{I}_M)) \text{diag}(\text{vec}(\mathbf{Q} \otimes \mathbf{F}_M)) \text{vec}(\bar{\Phi} \otimes \mathbf{1}_{M \times M}), \end{aligned} \quad (12)$$

where (f) follows from the vectorization identity as mentioned before, (g) follows from the mixed-product property of the

Kronecker and Hadamard products, i.e., $(\mathbf{A} \odot \mathbf{B}) \otimes (\mathbf{C} \odot \mathbf{D}) = (\mathbf{A} \otimes \mathbf{C}) \odot (\mathbf{B} \otimes \mathbf{D})$, and (h) follows from the vectorization identity of the Hadamard product, i.e., $\text{vec}(\mathbf{A} \odot \mathbf{B}) = \text{diag}(\text{vec}(\mathbf{A})) \text{vec}(\mathbf{B})$ [26].

Based on the above matrix transformations, an explicit linear representation of the cascaded channel \mathbf{h} with respect to $\text{vec}(\bar{\Phi} \otimes \mathbf{1}_{M \times M})$ is obtained. However, the coupling between $\mathbf{1}_{M \times M}$ and the unknown VR matrix $\bar{\Phi}$ is undesirable, as it masks the intrinsic sparsity structure of the VR. To address this issue, Lemma 1 is further invoked to decouple $\text{vec}(\bar{\Phi} \otimes \mathbf{1}_{M \times M})$ into $\mathbf{S}(\mathbf{1}_{M \times M}) \text{vec}(\bar{\Phi})$.

Lemma 1. For any matrices $\mathbf{A} = [\mathbf{a}_1, \dots, \mathbf{a}_{c_A}] \in \mathbb{C}^{r_A \times c_A}$ and $\mathbf{B} = [\mathbf{b}_1, \dots, \mathbf{b}_{c_B}] \in \mathbb{C}^{r_B \times c_B}$, there exists a transformation matrix $\mathbf{S}(\mathbf{A}) \in \mathbb{C}^{r_B c_B r_A c_A \times r_B c_B}$ such that

$$\text{vec}(\mathbf{B} \otimes \mathbf{A}) = \mathbf{S}(\mathbf{A}) \text{vec}(\mathbf{B}), \quad (13)$$

where $\mathbf{S}(\mathbf{A})$ is explicitly given by $\mathbf{S}(\mathbf{A}) = \mathbf{I}_{c_B} \otimes \begin{bmatrix} \mathbf{I}_{r_B} \otimes \mathbf{a}_1 \\ \vdots \\ \mathbf{I}_{r_B} \otimes \mathbf{a}_{c_A} \end{bmatrix}$.

Proof. The proof is omitted due to space limitation. \square

Using Lemma 1, the cascaded channel can be written as

$$\mathbf{h} = \mathbf{D}_2(\mathbf{x}) \text{vec}(\bar{\Phi}), \quad (14)$$

where $\mathbf{D}_2(\mathbf{x}) = (\mathbf{x}^T \otimes (\boldsymbol{\eta}^T \otimes \mathbf{I}_M)) \text{diag}(\text{vec}(\mathbf{Q} \otimes \mathbf{F}_M)) \mathbf{S}(\mathbf{1}_{M \times M})$. Thus, the cascaded channel \mathbf{h} is represented as a linear model with respect to the vectorized VR matrix $\text{vec}(\bar{\Phi})$.

Through these matrix transformations, two intuitive linear models, i.e., (11) and (14), are obtained. These models explicitly relate the original unknown parameters, namely, the far-field sparse matrix \mathbf{A} , the near-field VR matrix $\bar{\Phi}$, and the sparse gain vector \mathbf{b} to the received signal through the reduced-dimensional representations \mathbf{x} and $\bar{\Phi}$.

3) *Off-Grid Effect Correction:* It is important to note that the sparse representation introduced above relies on the assumption that the scatterer-, user-, and RIS-related angles or positions lie exactly on the predefined angular or polar grids. In practice, however, the spatial angles $\vartheta_{B,l}$ and $\varphi_{R,l}$, as well as the user/scatterer locations $[\vartheta_{U,l}, r_{U,l}]$, are continuous-valued, and the actual propagation parameters generally do not coincide with the discretized grids, leading to a basis mismatch. To mitigate this issue, off-grid vectors are introduced to refine the dictionary representation.

Specifically, let $m_l \triangleq \arg \min_m |\vartheta_{B,l} - \vartheta_m|$ and $q_l \triangleq \arg \min_q D([\bar{\varphi}_l, \bar{r}_l], [\bar{\varphi}_q, \bar{r}_q])$, for all $l \in \mathcal{L} \triangleq \{1, \dots, L_U L_{R_B}\}$, where m_l and q_l denote the indices of the predefined angular and polar grid points closest to $\vartheta_{B,l}$ and $[\bar{\varphi}_l, \bar{r}_l]$, respectively. Here, $D(\cdot, \cdot)$ is defined as $D([\bar{\varphi}_1, \bar{r}_1], [\bar{\varphi}_2, \bar{r}_2]) = \sqrt{\bar{r}_1^2 + \bar{r}_2^2 - 2\bar{r}_1\bar{r}_2 \cos(\phi_2 - \phi_1)}$, which characterizes the distance between two polar-domain points $(\bar{\varphi}_1, \bar{r}_1)$ and $(\bar{\varphi}_2, \bar{r}_2)$, with $\bar{\varphi}_1 = \arccos \bar{\varphi}_1$ and $\bar{\varphi}_2 = \arccos \bar{\varphi}_2$. Then, the off-grid vectors are defined as $\Delta \vartheta \triangleq [\Delta \vartheta_1, \dots, \Delta \vartheta_M]^T$, $\Delta \bar{\varphi} \triangleq$

$[\Delta\bar{\varphi}_1, \dots, \Delta\bar{\varphi}_{\bar{Q}}]^T$ and $\Delta\bar{\mathbf{r}} \triangleq [\Delta\bar{r}_1, \dots, \Delta\bar{r}_{\bar{Q}}]^T$, where $\Delta\vartheta_m$ ($\forall m \in \mathcal{M}$), $\Delta\bar{\varphi}_q$ and $\Delta\bar{r}_q$ ($\forall q \in \bar{\mathcal{Q}}$) are given by

$$\Delta\vartheta_m = \begin{cases} \vartheta_{B,l} - \vartheta_m, & \text{if } m = m_l, \\ 0, & \text{if } m \neq m_l, \end{cases} \quad (15)$$

$$\Delta\bar{\varphi}_q = \begin{cases} \bar{\varphi}_l - \bar{\varphi}_q, & \text{if } q = q_l, \\ 0, & \text{if } q \neq q_l, \end{cases} \quad \Delta\bar{r}_q = \begin{cases} \bar{r}_l - \bar{r}_q, & \text{if } q = q_l, \\ 0, & \text{if } q \neq q_l, \end{cases} \quad (16)$$

$\forall l \in \mathcal{L}$, respectively. For notational convenience, we define $\boldsymbol{\Xi} \triangleq \{\Delta\bar{\varphi}, \Delta\bar{\mathbf{r}}, \Delta\vartheta\}$ as the off-grid parameters set. By incorporating $\boldsymbol{\Xi}$, the resulting channel can be expressed as

$$\begin{aligned} \mathbf{h} &= (\boldsymbol{\eta}^T \otimes \mathbf{I}_M)((\mathbf{Q}(\Delta\bar{\varphi}, \Delta\bar{\mathbf{r}}) \odot \bar{\boldsymbol{\Phi}}) \otimes \mathbf{F}_M(\Delta\vartheta)) \mathbf{x} \\ &= (\mathbf{x}^T \otimes (\boldsymbol{\eta}^T \otimes \mathbf{I}_M)) \text{diag}(\text{vec}(\mathbf{Q}(\Delta\bar{\varphi}, \Delta\bar{\mathbf{r}}) \otimes \mathbf{F}_M(\Delta\vartheta))) \\ &\quad \times \mathbf{S}(\mathbf{1}_{M \times M}) \text{vec}(\bar{\boldsymbol{\Phi}}). \end{aligned} \quad (17)$$

In this way, the proposed model explicitly accounts for the off-grid deviations of the continuous propagation parameters from the predefined dictionaries, thereby mitigating basis mismatch and enabling an accurate sparse-domain representation of the cascaded channel.

B. Hierarchical Sparse Prior Model

To fully exploit the sparsity and structural characteristics of the cascaded sparse channel gain vector \mathbf{x} , it is essential to adopt a structure-aware probabilistic model. Motivated by [27], we employ a three-layer hierarchical sparse (3LHS) prior model. Different from two-layer priors that rely solely on either the support or the variance [28], [29], the 3LHS model jointly accounts for both components, providing a flexible and robust probabilistic representation. Prior works [30], [31] have shown that this model can naturally capture structured sparsity while maintaining low computational complexity, making it particularly suitable for modeling the cascaded channel in this work. Specifically, the 3LHS model consists of three layers, i.e., the support vector \mathbf{s} , the precision vector $\boldsymbol{\rho}$, and the sparse gain vector \mathbf{x} , with the joint distribution given by

$$p(\mathbf{x}, \boldsymbol{\rho}, \mathbf{s}) = p(\mathbf{s}) p(\boldsymbol{\rho}|\mathbf{s}) p(\mathbf{x}|\boldsymbol{\rho}). \quad (18)$$

Specifically, the support vector \mathbf{s} is introduced to indicate whether each element of the cascaded sparse channel gain vector \mathbf{x} is zero. In particular, $s_n = 0$ means that x_n is zero, while $s_n \neq 0$ indicates that x_n is nonzero. Moreover, by appropriately modeling the support vector \mathbf{s} , the unique sparse structure of \mathbf{x} can be effectively characterized. In the considered scenario, the cascaded sparse channel gain vector \mathbf{x} exhibits the following structural characteristics: \mathbf{h}_u contains L_U paths, while \mathbf{H} contains L_{RB} paths. Accordingly, the sparse matrix \mathbf{A} contains L_U nonzero elements, while the sparse vector \mathbf{b} contains L_{RB} nonzero elements. As a result, the equivalent sparse matrix \mathbf{X} contains $L_U L_{RB}$ nonzero elements. Furthermore, it is readily seen that each column of \mathbf{X} contains at most one nonzero element, indicating that each equivalent path on the RIS side corresponds to at most one AoD. This column-wise sparsity structure suggests that no explicit dependency needs to be imposed across different support entries. Therefore, modeling the support vector \mathbf{s} as independent and identically distributed (i.i.d.) provides a

sufficiently expressive yet parsimonious description of the sparsity pattern. Consequently, for \mathbf{s} , we have

$$\text{unvec}_{M \times \bar{Q}}(\mathbf{s}) = \begin{bmatrix} s_{1,1} & s_{1,2} & \cdots & s_{1,\bar{Q}} \\ s_{2,1} & s_{2,2} & \cdots & s_{2,\bar{Q}} \\ \vdots & \vdots & \ddots & \vdots \\ s_{M,1} & s_{M,2} & \cdots & s_{M,\bar{Q}} \end{bmatrix} \in \{0, 1\}, \quad (19)$$

and its probability distribution is given by

$$p(\mathbf{s}) = \prod_{m=1}^M \prod_{q=1}^{\bar{Q}} (\lambda_{m,q})^{s_{m,q}} (1 - \lambda_{m,q})^{1-s_{m,q}}, \quad (20)$$

where $\lambda_{m,q}$ is determined by the sparsity of \mathbf{x} . Moreover, the precision vector $\boldsymbol{\rho}$ controls the variance of \mathbf{x} , e.g., $1/\rho_{m,q}$ represents the variance of $x_{m,q}$. The conditional probability $p(\boldsymbol{\rho}|\mathbf{s})$ is given by

$$\begin{aligned} p(\boldsymbol{\rho}|\mathbf{s}) &= \prod_{m=1}^M \prod_{q=1}^{\bar{Q}} \Gamma(\rho_{m,q}; a_{m,q}, b_{m,q})^{s_{m,q}} \\ &\quad \times \Gamma(\rho_{m,q}; \bar{a}_{m,q}, \bar{b}_{m,q})^{1-s_{m,q}}, \end{aligned} \quad (21)$$

where $\Gamma(\rho; a, b)$ serves as a conjugate prior to enable closed-form posterior inference. Specifically, when $s_{m,q} = 1$, the inverse precision $1/\rho_{m,q}$ is expected to be close to 1, implying that the mean of $\rho_{m,q}$ satisfies $a_{m,q}/b_{m,q} = \mathbb{E}[\rho_{m,q}] = \Theta(1)$. Conversely, when $s_{m,q} = 0$, $1/\rho_{m,q}$ should be close to 0, which leads to a significantly larger mean, i.e., $\bar{a}_{m,q}/\bar{b}_{m,q} = \mathbb{E}[\rho_{m,q}] \gg 1$. Finally, based on the precision parameter $\boldsymbol{\rho}$, we model the cascaded sparse channel gain vector \mathbf{x} with a zero-mean complex Gaussian prior, whose variance is governed by the corresponding precision parameter, i.e.,

$$p(\mathbf{x}|\boldsymbol{\rho}) = \prod_{m=1}^M \prod_{q=1}^{\bar{Q}} \mathcal{CN}(x_{m,q}; 0, \rho_{m,q}^{-1}). \quad (22)$$

C. Markov Stationary Clustering Prior Model

As mentioned in Section II, 0/1 variables are employed to indicate whether each RIS element can reflect the user's signal, with all elements within the same subarray sharing identical visibility. To explicitly characterize the subarray-level visibility structure, we define the subarray VR matrix of the RIS as $\bar{\boldsymbol{\Phi}}_s \in \{0, 1\}^{K \times \bar{Q}}$. Based on this definition, the full-RIS VR matrix is $\bar{\boldsymbol{\Phi}} = \bar{\boldsymbol{\Phi}}_s \otimes \mathbf{1}_{\frac{N}{K} \times 1}$, where the subarray visibility is replicated across all elements in each subarray. Accordingly, the received signal model can be equivalently rewritten as

$$\mathbf{y} = \mathbf{D}_1(\bar{\boldsymbol{\Phi}}_s, \boldsymbol{\Xi})\mathbf{x} + \mathbf{n} = \mathbf{D}_2(\mathbf{x}, \boldsymbol{\Xi})\text{vec}(\bar{\boldsymbol{\Phi}}_s) + \mathbf{n}, \quad (23)$$

where $\mathbf{D}_1(\bar{\boldsymbol{\Phi}}_s, \boldsymbol{\Xi}) = (\boldsymbol{\eta}^T \otimes \mathbf{I}_M)((\mathbf{Q}(\Delta\bar{\varphi}, \Delta\bar{\mathbf{r}}) \odot (\bar{\boldsymbol{\Phi}}_s \otimes \mathbf{1}_{\frac{N}{K} \times 1})) \otimes \mathbf{F}_M(\Delta\vartheta))$ and $\mathbf{D}_2(\mathbf{x}, \boldsymbol{\Xi}) = (\mathbf{x}^T \otimes (\boldsymbol{\eta}^T \otimes \mathbf{I}_M)) \text{diag}(\text{vec}(\mathbf{Q}(\Delta\bar{\varphi}, \Delta\bar{\mathbf{r}}) \otimes \mathbf{F}_M(\Delta\vartheta))) \mathbf{S}(\mathbf{1}_{M \times M}) \mathbf{S}(\mathbf{1}_{\frac{N}{K} \times 1})$. To capture the spatial correlation across subarrays, a Markov chain is introduced to characterize the dependency of visibility between neighboring subarrays [25]. Accordingly, the prior distribution of the subarray VR matrix is given by

$$p(\bar{\boldsymbol{\Phi}}_s) = \prod_{q=1}^{\bar{Q}} p(v_{1,q}) \prod_{k=2}^K p(v_{k,q}|v_{k-1,q}). \quad (24)$$

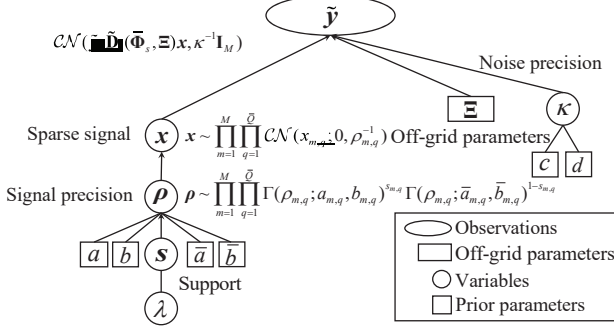


Fig. 2: Joint probabilistic model of the received signal.

Here, the initial and transition probabilities are defined as $p(v_{1,q} = 1) = \lambda_{VR}$ and $p(v_{k,q} = 1|v_{k-1,q} = 0) = p_{01}$, respectively, while the remaining transition probabilities p_{10} , p_{00} , and p_{11} are defined analogously and satisfy

$$p_{10} + p_{11} = 1, \quad p_{00} + p_{01} = 1, \quad \lambda_{VR} \triangleq \frac{p_{01}}{p_{01} + p_{10}}, \quad (25)$$

where λ_{VR} denotes the sparsity ratio of the VR, i.e., the proportion of RIS elements that are visible to the user. The last equality in (25) ensures that the Markov chain admits λ_{VR} as its steady-state probability.

D. Joint Probabilistic Model of the Received Signal

As shown in (6), the received signal \tilde{y} can be described by a linear observation model with additive noise. With the probabilistic model of the cascaded channel in place, we proceed to specify the statistical characterization of the noise component, i.e., $\tilde{\mathbf{n}}$. Specifically, the noise vector $\tilde{\mathbf{n}}$ is modeled as a complex Gaussian random vector, i.e., $\tilde{\mathbf{n}} \sim \mathcal{CN}(\mathbf{0}, \kappa^{-1} \mathbf{I})$, where κ denotes the noise precision. A Gamma prior is further assigned to the noise precision κ as $p(\kappa) = \Gamma(\kappa; c, d)$, where c and d are the corresponding hyperparameters. Then, the joint distribution of all latent variables and parameters, including the received signal \tilde{y} , the cascaded sparse channel gain vector \mathbf{x} , the subarray VR matrix $\bar{\Phi}_s$, the hierarchical sparse variables ρ and s , the off-grid parameters Ξ , and the noise precision κ , can be factorized as

$$p(\tilde{y}, \mathbf{x}, \bar{\Phi}_s, \Xi, \rho, s, \kappa) = p(\tilde{y}|\mathbf{x}, \bar{\Phi}_s, \kappa, \Xi) \times p(\mathbf{x}, \rho, s) p(\bar{\Phi}_s) p(\kappa), \quad (26)$$

where $p(\tilde{y}|\mathbf{x}, \bar{\Phi}_s, \kappa, \Xi)$ denotes the likelihood function. Specifically, conditioned on \mathbf{x} , $\bar{\Phi}_s$, Ξ and κ , the received signal \tilde{y} follows a complex Gaussian distribution given by

$$\tilde{y} \sim \mathcal{CN}(\tilde{\mathbf{D}}_1(\bar{\Phi}_s, \Xi)\mathbf{x}, \kappa^{-1} \mathbf{I}), \quad (27)$$

where $\tilde{\mathbf{D}}_1(\bar{\Phi}_s, \Xi)$ is constructed by row-wise concatenation of the sensing matrices corresponding to the P pilot symbols. $\tilde{\mathbf{D}}_2(\mathbf{x}, \Xi)$ is defined in an analogous manner. The structured sparse prior $p(\mathbf{x}, \rho, s)$, and the prior of the subarray VR matrix $p(\bar{\Phi}_s)$ are specified in Sections III-B and III-C. The resulting probabilistic dependencies among all variables are summarized in Fig. 2. Building upon the above probabilistic formulation, this work develops an efficient algorithm for estimating the cascaded channel parameters. To leverage both the structured

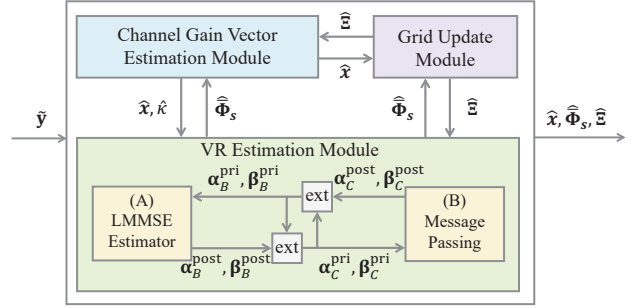


Fig. 3: Flow chart of the proposed algorithm.

sparsity of the channel and the probabilistic priors of the latent variables, a unified Bayesian inference framework is adopted. Within this framework, the TS-JBE algorithm is presented in the following section, which integrates the channel structure and prior information to jointly estimate the cascaded channel parameters.

IV. TURBO-STRUCTURED JOINT BAYESIAN ESTIMATION ALGORITHM

Owing to the bilinear structure of the received signal and the disparate forms of the prior and likelihood functions, direct joint maximum a posteriori (MAP) estimation of \mathbf{x} , $\bar{\Phi}_s$, and Ξ is intractable. To tackle this challenge, we develop the TS-JBE algorithm, which follows an alternating MAP inference framework to iteratively update the unknown parameters. In particular, the joint optimization problem is formulated as

$$(\mathbf{x}^*, \bar{\Phi}_s^*, \Xi^*) = \arg \max_{\mathbf{x}, \bar{\Phi}_s, \Xi} \ln p(\tilde{y}, \mathbf{x}, \bar{\Phi}_s, \Xi, \rho, s, \kappa). \quad (28)$$

A. Outline of the TS-JBE Algorithm

The proposed approach consists of three core modules, namely, the channel gain estimation module, the VR estimation module, and the grid update module, as illustrated in Fig. 3. These three modules operate alternately until convergence, and their functions are outlined below.

- **Channel Gain Estimation Module:** Given the current VR matrix $\hat{\bar{\Phi}}_s$ and the off-grid parameters $\hat{\Xi}$, this module jointly estimates the cascaded sparse channel gain vector \mathbf{x} and the noise precision κ by maximizing their posterior distribution. This step leverages the structured sparsity prior of the channel as established in (18) and the likelihood function determined by the received signal.
- **VR Estimation Module:** With the estimated cascaded sparse channel gain vector $\hat{\mathbf{x}}$ and off-grid parameters $\hat{\Xi}$ fixed, this module updates the subarray VR matrix $\bar{\Phi}_s$ to identify the visible RIS elements for each path, exploiting the prior information of the visibility pattern.
- **Grid Update Module:** To mitigate the off-grid mismatch, this module refines the off-grid parameters Ξ using a gradient descent step based on the residual error between the received signal \tilde{y} and its reconstruction from the current estimates of $\hat{\mathbf{x}}$ and $\hat{\bar{\Phi}}_s$.

B. Channel Gain Vector Estimation Module

Given $\tilde{\mathbf{y}}$, $\hat{\Phi}_s$ and $\hat{\Xi}$, the cascaded sparse channel gain vector \mathbf{x} and the noise precision κ are inferred via MAP estimation. Specifically, their estimates are given by

$$\begin{aligned}\mathbf{x}^* &= \arg \max_{\mathbf{x}} p(\mathbf{x}|\tilde{\mathbf{y}}, \hat{\Phi}_s, \hat{\Xi}), \\ \kappa^* &= \arg \max_{\kappa} p(\kappa|\tilde{\mathbf{y}}, \hat{\Phi}_s, \hat{\Xi}),\end{aligned}\quad (29)$$

respectively, where $p(\mathbf{x}|\tilde{\mathbf{y}}, \hat{\Phi}_s, \hat{\Xi})$ and $p(\kappa|\tilde{\mathbf{y}}, \hat{\Phi}_s, \hat{\Xi})$ denote the posterior distributions of \mathbf{x} and κ , respectively. According to the joint distribution in (26), the joint estimation of \mathbf{x} and κ constitutes a high-dimensional Bayesian inference problem involving multiple probabilistically coupled latent variables, including ρ and s . To enable efficient and tractable posterior inference while exploiting the structured sparsity of \mathbf{x} , a structured-subspace-constrained variational Bayesian inference (SSC-VBI) method is developed to infer \mathbf{x} and κ .

Different from existing VBI-based sparse estimation methods, such as SC-VBI [31], the proposed SSC-VBI explicitly incorporates the structured sparsity and subspace constraints of the cascaded channel into the variational inference framework. By exploiting the structural characteristics of the channel to optimize the subspace selection strategy, SSC-VBI achieves more robust and efficient posterior estimation in high-dimensional sparse scenarios, making it particularly suited for structured channel estimation. For notational simplicity, let ψ_j denote an individual variable in the set $\Psi \triangleq \{\mathbf{x}, \rho, s, \kappa\}$, and define the index set $\mathcal{H} \triangleq \{j | \psi_j \in \Psi\}$. Let $p(\Psi|\tilde{\mathbf{y}})$ denote the posterior distribution of Ψ , with $\hat{\Phi}_s$ and $\hat{\Xi}$ treated as fixed in the observation matrix $\tilde{\mathbf{D}}_1 \triangleq \tilde{\mathbf{D}}_1(\hat{\Phi}_s, \hat{\Xi})$. According to the VBI method, the approximate posterior $q(\Psi)$ is obtained by minimizing the KL-divergence (KLD) between $p(\Psi|\tilde{\mathbf{y}})$ and $q(\Psi)$ subject to a factorized form constraint, following [29],

$$\begin{aligned}\mathcal{A}_{\text{VBI}} : \quad & \min_{q(\Psi)} \int q(\Psi) \ln \frac{q(\Psi)}{p(\Psi|\tilde{\mathbf{y}})} d\Psi \\ & \text{s.t. } q(\Psi) = \prod_{j \in \mathcal{H}} q(\psi_j), \int q(\psi_j) d\psi_j = 1.\end{aligned}\quad (30)$$

Since the KLD in \mathcal{A}_{VBI} is convex with respect to each individual variable ψ_j while keeping all other variational distributions fixed, the variational distributions can be updated in an alternating manner to obtain a stationary solution, with the update rule given by

$$q(\psi_j) = \frac{\exp \left(\langle \ln p(\Psi, \tilde{\mathbf{y}}) \rangle_{\prod_{k \neq j} q(\psi_k)} \right)}{\int \exp \left(\langle \ln p(\Psi, \tilde{\mathbf{y}}) \rangle_{\prod_{k \neq j} q(\psi_k)} \right) d\psi_j}. \quad (31)$$

Clearly, according to the above update rule, updating $q(\mathbf{x})$ requires computing high-dimensional matrix inverses. To alleviate this computational burden, the SC-VBI algorithm introduces an additional structural constraint on the variational optimization problem \mathcal{A}_{VBI} , namely,

$$q(\mathbf{x}) = \mathcal{CN}(\mathbf{x}; \boldsymbol{\mu}, \text{diag}(\boldsymbol{\sigma}^2)), \quad (32)$$

where $\boldsymbol{\sigma}^2 = [\sigma_1^2, \sigma_2^2, \dots, \sigma_{M\bar{Q}}^2]^T$. This constraint enforces independence among the sparse vector elements, yielding a diagonal posterior covariance and eliminating high-dimensional

matrix inversion, since the structural dependencies of \mathbf{x} are explicitly captured by the latent variable s in the 3LHS model. Based on the variational optimization problem (30) with the additional constraint (32), and the update rule (31), the variational posterior updates are given as follows.

1) *Update Equation for \mathbf{x} :* Based on Lemma 2 in [31], the variational posterior of \mathbf{x} takes the form

$$q(\mathbf{x}) = \mathcal{CN}(\mathbf{x}; \boldsymbol{\mu}, \text{diag}(\boldsymbol{\sigma}^2)), \quad (33)$$

where $\boldsymbol{\mu} = \mathbf{G}^{-1} \tilde{\mathbf{D}}_1^H \tilde{\mathbf{y}}$, $\boldsymbol{\sigma}^2 = [G_1^{-1}, G_2^{-1}, \dots, G_{M\bar{Q}}^{-1}]$, with $\mathbf{G} = \text{diag}(\langle \boldsymbol{\rho} \rangle) + \langle \kappa \rangle \tilde{\mathbf{D}}_1^H \tilde{\mathbf{D}}_1$.

2) *Update Equation for $\boldsymbol{\rho}$:* $q(\boldsymbol{\rho})$ can be derived as

$$q(\boldsymbol{\rho}) = \prod_{m=1}^M \prod_{q=1}^{\bar{Q}} \Gamma(\rho_{m,q}; \tilde{a}_{m,q}, \tilde{b}_{m,q}), \quad (34)$$

where $\tilde{a}_{m,q} = \langle s_{m,q} \rangle a_{m,q} + \langle 1 - s_{m,q} \rangle a_{m,q} + 1$, $\tilde{b}_{m,q} = \langle s_{m,q} \rangle b_{m,q} + \langle 1 - s_{m,q} \rangle b_{m,q} + \langle |x_{m,q}|^2 \rangle$.

3) *Update Equation for s :* The posterior distribution $q(s)$ is given by

$$q(s) = \prod_{m=1}^M \prod_{q=1}^{\bar{Q}} (\tilde{\lambda}_{m,q})^{s_{m,q}} (1 - \tilde{\lambda}_{m,q})^{1-s_{m,q}}. \quad (35)$$

4) *Update Equation for κ :* The variational posterior of κ can be derived as

$$q(\kappa) = \Gamma(\kappa; \tilde{c}, \tilde{d}), \quad (36)$$

where $\tilde{c} = c + MP$, $\tilde{d} = d + \langle \|\tilde{\mathbf{y}} - \tilde{\mathbf{D}}_1 \mathbf{x}\|^2 \rangle_{q(\mathbf{x})}$. Besides exploiting the above independence to eliminate matrix inversion in the posterior covariance $\boldsymbol{\sigma}^2$, the sparsity of \mathbf{x} is further leveraged to identify an active index set, thereby avoiding high-dimensional matrix inversion in the posterior mean $\boldsymbol{\mu}$ update. Specifically, based on the identified active index set S_μ obtained in the last iteration, the posterior mean of \mathbf{x} in the i_x -th iteration ($i_x \in \mathcal{I}_x \triangleq \{1, 2, \dots, I_x\}$) is first updated as

$$\mathbf{u}_{i_x}^{(0)}(S_\mu) = \langle \kappa \rangle \mathbf{G}(S_\mu, S_\mu)^{-1} \tilde{\mathbf{D}}_1(:, S_\mu)^H \tilde{\mathbf{y}}. \quad (37)$$

To refine the estimation, the SC-VBI algorithm takes $\mathbf{u}_{i_x}^{(0)}$ as the initial solution to the following optimization problem

$$\min_{\mathbf{u}} \varphi(\mathbf{u}) \triangleq \mathbf{u}^H \mathbf{G} \mathbf{u} - 2 \Re \left\{ \mathbf{u}^H \tilde{\mathbf{D}}_1^H \tilde{\mathbf{y}} \right\}, \quad (38)$$

which is equivalent to minimizing the KLD with respect to \mathbf{x} while keeping all other variational parameters fixed, according to the update rule in (31). A gradient-based update scheme is then applied to iteratively refine \mathbf{u} , given by

$$\mathbf{u}_{i_x}^{(i_g)} = \mathbf{u}_{i_x}^{(i_g-1)} - \epsilon^{(i_g)} \nabla_{\mathbf{u}} \varphi(\mathbf{u}) \Big|_{\mathbf{u}=\mathbf{u}_{i_x}^{(i_g-1)}}, \quad (39)$$

where $i_g \in \mathcal{I}_g \triangleq \{1, \dots, I_g\}$ denotes the index of the gradient descent iteration, and $\epsilon^{(i_g)}$ is the corresponding step size. Accordingly, the resulting $\boldsymbol{\mu}^{(i_x)} \triangleq \mathbf{u}_{i_x}^{(I_g)}$ serves as the posterior mean estimate of \mathbf{x} .

In the considered problem, the sparse vector \mathbf{x} exhibits a column-wise sparsity pattern, where each column contains at most one nonzero element. Motivated by this observation,

we refine the SC-VBI by explicitly incorporating the column-wise sparsity structure of \mathbf{x} to guide the construction of the subspace index set, thereby improving the estimation accuracy. Specifically, let $\boldsymbol{\mu}^{(i_x-1)}$ denote the posterior mean vector obtained at the $(i_x - 1)$ -th iteration. By reshaping $\boldsymbol{\mu}^{(i_x-1)}$ into matrix form as $\mathbf{U}^{(i_x-1)} \triangleq \text{unvec}_{M \times \bar{Q}}(\boldsymbol{\mu}^{(i_x-1)})$, the active columns are identified according to an energy-based thresholding criterion as follows:

$$\mathcal{Q}_{\boldsymbol{\mu}^{(i_x-1)}} \triangleq \left\{ q \in \bar{\mathcal{Q}} \mid \|\mathbf{U}_{:,q}^{(i_x-1)}\|^2 > \varepsilon_\mu \right\}, \quad (40)$$

where the threshold ε_μ is chosen such that the selected columns in $\mathcal{Q}_{\boldsymbol{\mu}^{(i_x-1)}}$ account for a dominant portion of the total energy of $\mathbf{U}^{(i_x-1)}$, e.g., no less than 95%. For each active column $q \in \mathcal{Q}_{\boldsymbol{\mu}^{(i_x-1)}}$, the dominant row index is selected as $m_q = \arg \max_m |\mathbf{U}_{m,q}^{(i_x-1)}|$. Accordingly, the final subspace index set is then defined as

$$S_\mu \triangleq \left\{ (q-1)M + m_q \mid q \in \mathcal{Q}_{\boldsymbol{\mu}^{(i_x-1)}} \right\}. \quad (41)$$

The posterior mean vector $\boldsymbol{\mu}^{(i_x)}$ is then updated only over the indices in (41), followed by refinement through the update rules in (37) and (39).

C. VR Estimation Module

Given $\bar{\mathbf{y}}$, $\hat{\mathbf{x}}$, $\hat{\boldsymbol{\Xi}}$ and $\hat{\kappa}$ obtained from the channel gain estimation module, the subarray VR matrix $\bar{\Phi}_s$ is also estimated under the MAP approach according to the linear observation model

$$\bar{\mathbf{y}} = \tilde{\mathbf{D}}_2(\hat{\mathbf{x}}, \hat{\boldsymbol{\Xi}})\text{vec}(\bar{\Phi}_s) + \tilde{\mathbf{n}} = \tilde{\mathbf{D}}_2\text{vec}(\bar{\Phi}_s) + \tilde{\mathbf{n}}, \quad (42)$$

where $\tilde{\mathbf{D}}_2 \triangleq \tilde{\mathbf{D}}_2(\hat{\mathbf{x}}, \hat{\boldsymbol{\Xi}})$. With this model, a turbo approach is employed for VR estimation, which iteratively exchanges extrinsic information between the linear Gaussian observation model and the structure-aware VR prior to achieve reliable estimation performance. Specifically, the proposed approach consists of two interconnected submodules: one incorporates the structural prior of the VR via a message passing (MP) algorithm, while the other updates the VR posterior distribution according to the current observation model. Through iterative information exchange between these two submodules, the proposed approach reliably estimates the VR while capturing its sparsity and structural dependencies.

1) *Preprocessing and Reformulation*: Before introducing the specific estimation module, the target VR and corresponding observation model are reformulated by exploiting the sparsity of $\hat{\mathbf{x}}$ and the real-valued nature of the VR. Firstly, due to the sparsity of \mathbf{x} , only a few columns in $\bar{\Phi}_s$ contribute to the channel. To reduce computational complexity, VR estimation is therefore restricted to these dominant columns. This restriction is embedded within an alternating inference framework, in which \mathbf{x} and $\bar{\Phi}_s$ are alternately refined, thereby avoiding the adverse effects caused by the fixation on early-stage estimates of \mathbf{x} . Specifically, the active column index set is determined from $\hat{\mathbf{x}}$ as in Section IV-B, denoted by $\mathcal{Q}_v \triangleq \mathcal{Q}_{\boldsymbol{\mu}^{(i_x)}}$. Accordingly, VR estimation is performed only on the corresponding subarray VR matrix $\bar{\Phi}_{s,\mathcal{Q}_v} = \bar{\Phi}_s(:, \mathcal{Q}_v) \in \mathbb{R}^{K \times |\mathcal{Q}_v|}$, with the corresponding selected measurement matrix $\tilde{\mathbf{D}}_{2,\mathcal{Q}_v}$.

Since $\bar{\Phi}_{s,\mathcal{Q}_v}$ is real-valued, the model is converted to an equivalent real-valued form $\bar{\mathbf{y}} = [\Re[\bar{\mathbf{y}}]^T, \Im[\bar{\mathbf{y}}]^T]^T$, with $\bar{\mathbf{D}}_{2,\mathcal{Q}_v}$ and $\bar{\mathbf{n}}$ defined accordingly, yielding the real-valued mode

$$\bar{\mathbf{y}} = \bar{\mathbf{D}}_{2,\mathcal{Q}_v}\text{vec}(\bar{\Phi}_{s,\mathcal{Q}_v}) + \bar{\mathbf{n}}. \quad (43)$$

With this reformulation, the VR estimation problem is cast into an equivalent compressed real-valued inference form, and a turbo approach consisting of two interconnected modules is developed to estimate the submatrix $\bar{\Phi}_{s,\mathcal{Q}_v}$. Specifically, an LMMSE module performs linear estimation under the transformed observation model, while an MP module exploits the structural characteristics of the VR. By iteratively exchanging information between these two modules, reliable and accurate VR estimation is achieved.

2) *Module A*: In Module A, the LMMSE estimator incorporates the prior information provided by the MP module to construct a Gaussian prior for \mathbf{x} and subsequently obtain the LMMSE estimate. Specifically, the prior mean and variance vectors $\boldsymbol{\alpha}_{A,pri}$ and $\boldsymbol{\beta}_{A,pri}$ are first received and used to model the submatrix $\bar{\Phi}_{s,\mathcal{Q}_v}$ as a Gaussian random vector. Accordingly, the prior distribution of $\bar{\Phi}_{s,\mathcal{Q}_v}$ is $\mathcal{N}(\text{vec}(\bar{\Phi}_{s,\mathcal{Q}_v}); \boldsymbol{\alpha}_{A,pri}, \text{diag}(\boldsymbol{\beta}_{A,pri}))$. At the first iteration, $\boldsymbol{\alpha}_{A,pri}$ and $\boldsymbol{\beta}_{A,pri}$ are initialized in an unbiased manner. Given the above prior model and the transformed observation model, the posterior distribution of $\bar{\Phi}_{s,\mathcal{Q}_v}$ can be obtained according to the LMMSE estimation principle. The resulting posterior covariance matrix and mean vector are respectively expressed as

$$\boldsymbol{\Gamma}_{A,post} = \left(\hat{\kappa} \bar{\mathbf{D}}_{2,\mathcal{Q}_v}^T \bar{\mathbf{D}}_{2,\mathcal{Q}_v} + \text{diag}\left(\frac{1}{\boldsymbol{\beta}_{A,pri}}\right) \right)^{-1}, \quad (44)$$

$$\boldsymbol{\alpha}_{A,post} = \boldsymbol{\Gamma}_{A,post} \left(\frac{\boldsymbol{\alpha}_{A,pri}}{\boldsymbol{\beta}_{A,pri}} + \hat{\kappa} \bar{\mathbf{D}}_{2,\mathcal{Q}_v}^T \bar{\mathbf{y}} \right). \quad (45)$$

Following the turbo processing principle, the posterior statistics obtained in this module cannot be directly forwarded to the subsequent message-passing module, since they are correlated with the prior information. To generate extrinsic information, a de-correlation operation is therefore applied [32]. The resulting prior mean and variance for Module B are given by

$$\boldsymbol{\alpha}_{B,pri} = \boldsymbol{\beta}_{B,pri} \left(\frac{\boldsymbol{\alpha}_{A,post}}{\boldsymbol{\beta}_{A,post}} - \frac{\boldsymbol{\alpha}_{A,pri}}{\boldsymbol{\beta}_{A,pri}} \right), \quad (46)$$

$$\boldsymbol{\beta}_{B,pri} = \left(\frac{1}{\boldsymbol{\beta}_{A,post}} - \frac{1}{\boldsymbol{\beta}_{A,pri}} \right)^{-1}. \quad (47)$$

3) *Module B*: In Module B, the MP estimator is built upon the LMMSE estimates by incorporating prior information on the structural characteristics of the VR, thereby achieving improved estimation performance. Specifically, the prior mean and variance vectors $\boldsymbol{\alpha}_{B,pri}$ and $\boldsymbol{\beta}_{B,pri}$ are interpreted as equivalent noisy observations of the binary VR variables, which are modeled as

$$\boldsymbol{\alpha}_{B,pri} = \text{vec}(\bar{\Phi}_{s,\mathcal{Q}_v}) + \mathbf{z}, \quad \mathbf{z} \sim \mathcal{N}(\mathbf{0}, \text{diag}(\boldsymbol{\beta}_{B,pri})). \quad (48)$$

Based on the above model, the joint distribution of $\boldsymbol{\alpha}_{B,pri}$ and $\bar{\Phi}_{s,\mathcal{Q}_v}$ can be expressed as

$$p(\boldsymbol{\alpha}_{B,pri}, \bar{\Phi}_{s,\mathcal{Q}_v}) = p(\bar{\Phi}_{s,\mathcal{Q}_v}) \prod_{k=1}^K \prod_{q=1}^{|\mathcal{Q}_v|} p(\alpha_{B,k,q}^{pri} | v_{k,q}), \quad (49)$$

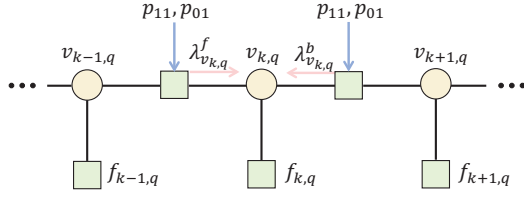


Fig. 4: Factor graph of the subarray VR for the q -th column.

where the prior distribution of $\bar{\Phi}_{s,\mathcal{Q}_v}$ follows

$$p(\bar{\Phi}_{s,\mathcal{Q}_v}) = \prod_{q=1}^{|\mathcal{Q}_v|} p(v_{1,q}) \prod_{k=2}^K p(v_{k,q}|v_{k-1,q}). \quad (50)$$

According to (50), the corresponding factor graph is illustrated in Fig. 4. For each factor node, the associated likelihood function is given by

$$f_{k,q} \triangleq \mathcal{N}\left(v_{k,q}; \alpha_{B,k,q}^{pri}, \beta_{B,k,q}^{pri}\right), k \in \{1, \dots, K\}, q \in \mathcal{Q}_v. \quad (51)$$

Following the sum-product rule, the forward and backward messages of node $v_{k,q}$, denoted by $\lambda_{v_{k,q}}^f$ and $\lambda_{v_{k,q}}^b$, respectively, are updated according to (53) and (54), as shown at the top of the next page, where the extrinsic input activation probability $\pi_{v,k,q}^{in}$ is given by

$$\pi_{v,k,q}^{in} = \frac{\mathcal{N}(1; \alpha_{B,k,q}^{pri}, \beta_{B,k,q}^{pri})}{\mathcal{N}(1; \alpha_{B,k,q}^{pri}, \beta_{B,k,q}^{pri}) + \mathcal{N}(0; \alpha_{B,k,q}^{pri}, \beta_{B,k,q}^{pri})}. \quad (52)$$

By combining the forward and backward messages, the extrinsic output activation probability is obtained as

$$\pi_{v,k,q}^{out} = \frac{\lambda_{v,k,q}^f \lambda_{v,k,q}^b}{(1 - \lambda_{v,k,q}^f)(1 - \lambda_{v,k,q}^b) + \lambda_{v,k,q}^f \lambda_{v,k,q}^b}. \quad (55)$$

At this stage, the posterior probability of $v_{k,q} = 1$ is then computed as

$$\hat{p}(v_{k,q} = 1) = \frac{\pi_{v,k,q}^{in} \pi_{v,k,q}^{out}}{\pi_{v,k,q}^{in} \pi_{v,k,q}^{out} + (1 - \pi_{v,k,q}^{in})(1 - \pi_{v,k,q}^{out})}. \quad (56)$$

Accordingly, the posterior mean and variance of $v_{k,q}$ are computed as

$$\alpha_{B,k,q}^{post} = \sum_{a \in \{0,1\}} a \hat{p}(v_{k,q} = a), \quad (57)$$

$$\beta_{B,k,q}^{post} = \sum_{a \in \{0,1\}} (a - \alpha_{B,k,q}^{post})^2 \hat{p}(v_{k,q} = a). \quad (58)$$

Similar to Module A, the posterior statistics are further processed to generate extrinsic information before being fed back to the LMMSE module. The corresponding extrinsic mean and variance are given by

$$\alpha_{A,k,q}^{pri} = \beta_{A,k,q}^{pri} \left(\frac{\alpha_{B,k,q}^{post}}{\beta_{B,k,q}^{post}} - \frac{\alpha_{B,k,q}^{pri}}{\beta_{B,k,q}^{pri}} \right), \quad (59)$$

$$\beta_{A,k,q}^{pri} = \left(\frac{1}{\beta_{B,k,q}^{post}} - \frac{1}{\beta_{B,k,q}^{pri}} \right)^{-1}. \quad (60)$$

Finally, a binary decision on $\bar{\Phi}_{s,\mathcal{Q}_v}$ is obtained by thresholding the posterior probability at 0.5, and the fully subarray VR matrix $\hat{\Phi}_s$ is reconstructed by setting $\hat{\Phi}_s(:, \mathcal{Q}_v) = \bar{\Phi}_{s,\mathcal{Q}_v}$.

D. Grid Update Module

Given the estimated VR $\hat{\Phi}_s$ and the cascaded channel gain $\hat{\mathbf{x}}$, the off-grid parameters Ξ are refined by solving the following maximum-likelihood (ML) problem:

$$\begin{aligned} \max_{\Delta\bar{\varphi}, \Delta\bar{r}, \Delta\vartheta} L(\Delta\bar{\varphi}, \Delta\bar{r}, \Delta\vartheta) = & - \sum_{p=1}^P \left\| \mathbf{y}_p - (\boldsymbol{\eta}_p^T \otimes \mathbf{I}_M) \right. \\ & \times ((\mathbf{Q}(\Delta\bar{\varphi}, \Delta\bar{r}) \odot \hat{\Phi}) \\ & \left. \otimes \mathbf{F}_M(\Delta\vartheta)) \hat{\mathbf{x}} \right\|^2, \end{aligned} \quad (61)$$

where $\hat{\Phi} \triangleq \hat{\Phi}_s \otimes \mathbf{1}_{\frac{N}{K} \times 1}$. For convenience, define $\mathbf{F}_p \triangleq \boldsymbol{\eta}_p^T \otimes \mathbf{I}_M$, $\bar{\mathbf{F}}_M \triangleq \mathbf{F}_M(\Delta\vartheta)$, and $\bar{\mathbf{Q}}_V \triangleq \mathbf{Q}(\Delta\bar{\varphi}, \Delta\bar{r}) \odot \hat{\Phi}$. Then, the objective function of problem (61) can be rewritten as

$$L(\Delta\bar{\varphi}, \Delta\bar{r}, \Delta\vartheta) = - \sum_{p=1}^P \left\| \mathbf{y}_p - \mathbf{F}_p(\bar{\mathbf{Q}}_V \otimes \bar{\mathbf{F}}_M) \hat{\mathbf{x}} \right\|^2. \quad (62)$$

To facilitate computing the derivatives of $L(\Delta\bar{\varphi}, \Delta\bar{r}, \Delta\vartheta)$ with respect to the off-grid set Ξ , we introduce intermediate terms. For the q -th near-field angular component, define

$$\begin{aligned} \mathbf{y}_p^{(\Delta\bar{\varphi}_q)} &= ((\mathbf{a}_q^{(\bar{\varphi}_q)} \odot \hat{\phi}_q) \otimes \bar{\mathbf{F}}_M)^H \mathbf{F}_p^H \mathbf{y}, \\ \mathbf{z}_p^{(\Delta\bar{\varphi}_q)} &= ((\mathbf{a}_q^{(\bar{\varphi}_q)} \odot \hat{\phi}_q) \otimes \bar{\mathbf{F}}_M)^H \mathbf{F}_p^H \mathbf{F}_p (\bar{\mathbf{Q}}_V \otimes \bar{\mathbf{F}}_M) \hat{\mathbf{x}}. \end{aligned} \quad (63)$$

Let the derivative of the ARV \mathbf{a}_q with respect to the off-grid angular perturbation $\Delta\bar{\varphi}_q$ be $\mathbf{a}_q^{(\Delta\bar{\varphi}_q)} = \frac{\partial \mathbf{a}([\bar{\varphi}_q + \Delta\bar{\varphi}_q, \bar{r}_q])}{\partial \Delta\bar{\varphi}_q}$. Using the above intermediate terms, the gradient of $L(\Delta\bar{\varphi}, \Delta\bar{r}, \Delta\vartheta)$ with respect to $\Delta\bar{\varphi}_q$ can be compactly written as

$$\frac{\partial L}{\partial \Delta\bar{\varphi}_q} = 2 \Re \sum_{p=1}^P \hat{\mathbf{x}}_{(q-1)M+1:qM}^H (\mathbf{y}_p^{(\Delta\bar{\varphi}_q)} - \mathbf{z}_p^{(\Delta\bar{\varphi}_q)}). \quad (64)$$

Similarly, the gradients with respect to $\Delta\bar{r}_q$ and $\Delta\vartheta_m$ can be derived respectively. Finally, the off-grid parameters are sequentially refined through gradient-based updates as follows:

$$\Delta\bar{\varphi}^{(i+1)} = \Delta\bar{\varphi}^{(i)} - \varepsilon_{\bar{\varphi}} \frac{\partial L(\Delta\bar{\varphi}^{(i)}, \Delta\bar{r}^{(i)}, \Delta\vartheta^{(i)})}{\partial \Delta\bar{\varphi}^{(i)}}, \quad (65)$$

$$\Delta\bar{r}^{(i+1)} = \Delta\bar{r}^{(i)} - \varepsilon_{\bar{r}} \frac{\partial L(\Delta\bar{\varphi}^{(i+1)}, \Delta\bar{r}^{(i)}, \Delta\vartheta^{(i)})}{\partial \Delta\bar{r}^{(i)}}, \quad (66)$$

$$\Delta\vartheta^{(i+1)} = \Delta\vartheta^{(i)} - \varepsilon_{\vartheta} \frac{\partial L(\Delta\bar{\varphi}^{(i+1)}, \Delta\bar{r}^{(i+1)}, \Delta\vartheta^{(i)})}{\partial \Delta\vartheta^{(i)}}, \quad (67)$$

where the step sizes $\varepsilon_{\bar{\varphi}}$, $\varepsilon_{\bar{r}}$, and ε_{ϑ} are adaptively selected via a backtracking line search [33].

E. Complexity Analysis

We summarize the proposed TS-JBE approach in Algorithm 1. In the channel gain vector estimation module, SSC-VBI avoids large-scale matrix inversion by restricting the operation to a reduced subspace of size $\mathbb{C}^{|S_\mu| \times |S_\mu|}$, combined with several matrix–vector multiplications, achieving a per-iteration complexity of $\mathcal{O}(M^2 \bar{Q} + |S_\mu|^3)$. In the VR estimation module, LMMSE estimator requires a matrix inversion of size $\mathbb{C}^{(K|\mathcal{Q}_v|) \times (K|\mathcal{Q}_v|)}$, resulting in a complexity of $\mathcal{O}((K|\mathcal{Q}_v|)^3)$, whereas the MP update exhibits linear complexity. In the grid update module, the dominant cost arises from computing

$$\lambda_{v,k,q}^f = \begin{cases} \lambda_{VR}, & k = 1, \\ \frac{p_{01}(1 - \pi_{v,k-1,q}^{in})(1 - \lambda_{v,k-1,q}^f) + p_{11}\pi_{v,k-1,q}^{in}\lambda_{v,k-1,q}^f}{(1 - \pi_{v,k-1,q}^{in})(1 - \lambda_{v,k-1,q}^f) + \pi_{v,k-1,q}^{in}\lambda_{v,k-1,q}^f}, & k > 1, \end{cases} \quad (53)$$

$$\lambda_{v,k,q}^b = \begin{cases} 0.5, & k = K, \\ \frac{p_{10}(1 - \pi_{v,k+1,q}^{in})(1 - \lambda_{v,k+1,q}^b) + p_{11}\pi_{v,k+1,q}^{in}\lambda_{v,k+1,q}^b}{(p_{00} + p_{10})(1 - \pi_{v,k+1,q}^{in})(1 - \lambda_{v,k+1,q}^b) + (p_{11} + p_{01})\pi_{v,k+1,q}^{in}\lambda_{v,k+1,q}^b}, & k < K. \end{cases} \quad (54)$$

Algorithm 1 Proposed TS-JBE algorithm

Input: receive signal $\tilde{\mathbf{y}}$, outer iterations I_{out} , channel vector iteration number I_x , VR iteration number I_v , gradient update iteration number I_g .

Output: channel sparse vector $\hat{\mathbf{x}}$, VR matrix $\hat{\Phi}_s$, off-grid parameters $\hat{\Xi}$.

- 1: **For** $i_{out} = 1, \dots, I_{out}$
- 2: Initialize $q(\mathbf{s}), q(\boldsymbol{\rho}), q(\boldsymbol{\kappa})$.
- 3: **Channel Gain Estimation Module**
- 4: **For** $i_x = 1, \dots, I_x$
- 5: Update $q(\mathbf{x})$ using (33), where the posterior mean $\boldsymbol{\mu}$ is obtained by performing the gradient update (39) with the initial point from (37) and (41) for I_g times.
- 6: Update $q(\boldsymbol{\rho})$ using (34).
- 7: Update $q(\mathbf{s})$ using (35).
- 8: Update $q(\boldsymbol{\kappa})$ using (36).
- 9: **end For**
- 10: Estimate $\hat{\mathbf{x}} = \boldsymbol{\mu}^{(I_x)}, \hat{\boldsymbol{\kappa}} = \frac{\tilde{\mathbf{c}}}{\tilde{d}}$.
- 11: Transform receive signal model as (43).
- 12: **VR Estimation Module**
- 13: **For** $i_v = 1, \dots, I_v$
- 14: **%Module A: LMMSE**
- 15: Compute $\boldsymbol{\Gamma}_A^{post}, \boldsymbol{\alpha}_A^{post}$ using (44) and (45).
- 16: Compute $\boldsymbol{\alpha}_B^{pri}, \boldsymbol{\beta}_B^{pri}$ using (46) and (47).
- 17: **%Module B: MP**
- 18: Compute $\pi_{v,k,q}^{in}$ using (52).
- 19: Compute $\lambda_{v,k,q}^f, \lambda_{v,k,q}^b$ using (53) and (54).
- 20: Compute $\pi_{v,k,q}^{out}$ using (55).
- 21: Compute $\boldsymbol{\alpha}_B^{post}, \boldsymbol{\beta}_B^{post}$ using (57) and (58).
- 22: Compute $\boldsymbol{\alpha}_A^{pri}, \boldsymbol{\beta}_A^{pri}$ using (59) and (60).
- 23: Estimate $\hat{\Phi}_s$ using a 0.5 threshold.
- 24: **end For**
- 25: **Grid Update Module**
- 26: estimate $\hat{\Xi}$ using (65), (66) and (67).
- 27: **end For**

gradients with respect to the polar grid parameters $[\bar{\varphi}, \bar{r}]$, resulting in a complexity of $\mathcal{O}(\bar{Q}^2)$. Denoting the iteration numbers of the channel gain and VR modules by I_x and I_v , respectively, the overall per-outer-iteration complexity of TS-JBE is $\mathcal{O}(I_x(M^2\bar{Q} + |S_\mu|^3) + I_v(K|\mathcal{Q}_v|)^3 + \bar{Q}^2)$.

V. SIMULATION RESULTS

In this section, numerical results are provided to validate the effectiveness of the proposed TS-JBE algorithm. We consider

a RIS-assisted MIMO system operating at a carrier frequency of $f = 28$ GHz under the TDD mode. The BS is equipped with a ULA of $M = 16$ antennas with inter-element spacing $d = \frac{\lambda}{2}$. The RIS comprises $N = 128$ reflecting elements arranged as a ULA with the same spacing, and a single-antenna user is assumed. The BS and RIS are aligned along the y - and x -axes with reference positions $[-90\text{m}, -30\text{m}]^T$ and $[0\text{m}, 0\text{m}]^T$, respectively. The user's distance to the RIS is between 10 m and 20 m. Based on the array aperture and the carrier wavelength, the Rayleigh distance of the RIS is approximately 87.5 m. The distance from the BS to the RIS is about 95.2 m, indicating that the BS lies in the far-field of the RIS, whereas the user is located in the near-field region. This configuration is consistent with the considered hybrid-field propagation scenario. The large-scale path loss follows $PL = \alpha_{PL} + 10\beta_{PL} \log_{10}(d) + \xi_{PL}$ (dB), $\xi_{PL} \sim \mathcal{N}(0, \sigma_{PL}^2)$, with the model and parameters adopted from [34]. Unless stated otherwise, $L_{RB} = L_U = 3$ paths are considered, the polar-domain dictionary has $\bar{Q} = 256$ points, the RIS is split into $K = 8$ subarrays, the VR sparsity ratio is 0.875, and SNR is 20 dB. In this paper, the NMSE of the cascaded channel is adopted as the performance metric. The cascaded channel vector is defined as $\mathbf{h}_c = \text{vec}(\mathbf{H}\text{diag}(\mathbf{h}_u))$. Accordingly, the NMSE is defined as $\|\hat{\mathbf{h}}_c - \mathbf{h}_c\|^2/\|\mathbf{h}_c\|^2$, where $\hat{\mathbf{h}}_c = ((\mathbf{Q}(\Delta\bar{\varphi}, \Delta\bar{r}) \odot \hat{\Phi}) \otimes \mathbf{F}_M(\Delta\vartheta))\hat{\mathbf{x}}$ denotes the reconstructed cascaded channel vector. For performance comparison, we consider the following baseline algorithms:

- **OMP:** This method assumes that all RIS elements are visible to the signal and applies OMP to estimate the cascaded channel.
- **SBL:** Similar to OMP, but uses sparse Bayesian learning (SBL) for cascaded channel estimation.
- **RFSBL:** The robust fast SBL (RFSBL) algorithm estimates the cascaded sparse channel gains, VRs, and off-grid parameters through a two-stage procedure [20].
- **TS-JBE without VR estimation:** This benchmark employs the proposed TS-JBE algorithm while disabling the VR estimation module. Only the cascaded sparse channel gains and the off-grid parameters are estimated.
- **Oracle LS:** LS estimation with perfect knowledge of path distances, angles, scatterer locations, and VRs, serving as a performance lower bound.

Before presenting the performance results, Fig. 5 verifies the convergence of the considered algorithms. The proposed algorithm shows a rapid NMSE reduction in early iterations, converging to a stable value after around 25 iterations, with a monotonically decreasing trend indicating good stability. This

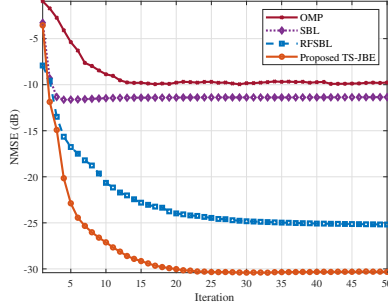


Fig. 5: Convergence behavior of the considered algorithms

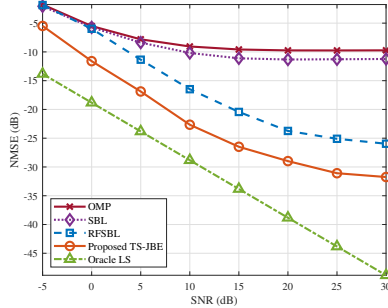


Fig. 6: NMSE performance of the considered algorithms versus SNR.

favorable convergence behavior stems from the proposed joint iterative approach, in which the cascaded sparse channel gains, VRs, and off-grid parameters are alternately updated, enabling consistent information exchange and progressive refinement across iterations. In comparison, SBL and OMP converge faster due to simpler iterative structures without joint VR and off-grid estimation, while RFSBL, also using multi-parameter alternating updates, converges more slowly, stabilizing after about 30 iterations.

Fig. 6 compares the NMSE performance of different algorithms under varying SNRs. As can be observed, estimation accuracy improves for all schemes as SNR increases. The proposed TS-JBE consistently outperforms OMP, SBL, and RFSBL across the entire SNR range. OMP and SBL do not consider non-stationarity or off-grid effects, causing performance to saturate in the medium-SNR regime, with little improvement beyond 15 dB. Both RFSBL and TS-JBE explicitly model the VR and off-grid effects, yielding much better performance than OMP and SBL. However, RFSBL's two-stage estimation is prone to error propagation, limiting its final accuracy. In contrast, TS-JBE employs joint estimation with a three-layer prior and Markov-structured constraints, providing stable gains and accurate characterization of the channel and VR structures. Compared with the Oracle LS benchmark, TS-JBE maintains an approximately constant gap in low-to-medium SNRs, demonstrating robustness to noise and stable estimation behavior.

Fig. 7 shows the NMSE performance of different algorithms versus the pilot number T . The NMSE of all schemes decreases monotonically as T increases. The proposed TS-JBE consistently outperforms all benchmarks when $T > 20$,

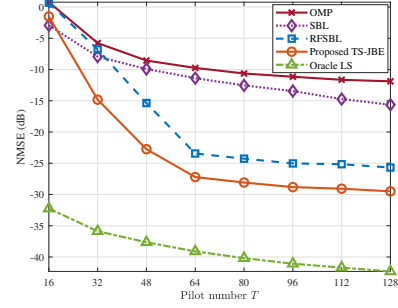


Fig. 7: NMSE performance under different pilot numbers.

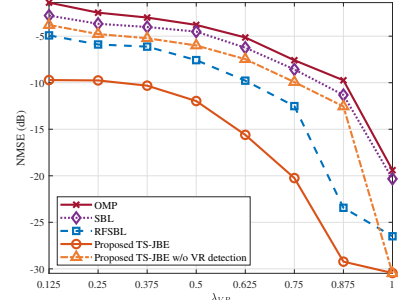


Fig. 8: NMSE performance under different VR sparsity ratios.

maintaining an advantage over RFSBL across the entire range. Beyond $T = 64$, its performance saturates, indicating that satisfactory estimation accuracy is achieved with 64 pilots. In contrast, OMP and SBL reduce NMSE much more slowly and perform significantly worse, as they do not account for channel non-stationarity and off-grid effects and thus cannot fully exploit longer pilot sequences.

Fig. 8 shows the NMSE performance of different algorithms under varying VR sparsity ratios λ_{VR} . As λ_{VR} increases, the NMSE of all schemes generally decreases due to richer observations from more visible RIS elements. Algorithms explicitly modeling the VR consistently outperform baselines assuming a fully visible RIS, such as OMP and SBL, highlighting the benefit of VR modeling. Among these, the proposed TS-JBE consistently maintains performance gains over RFSBL even under low visibility conditions, indicating the stability of the algorithm. Furthermore, incorporating VR estimation significantly improves performance in partially visible scenarios, whereas this gain disappears when $\lambda_{VR} = 1$, where all RIS elements are visible and explicit VR modeling is unnecessary.

VI. CONCLUSION

This paper investigated non-stationary cascaded channel estimation in RIS-assisted millimeter-wave systems under a hybrid-field propagation environment. Exploiting the cascaded channel structure, a compression strategy based on a visibility-matrix-weighted low-dimensional polar-domain dictionary was designed to construct a reduced-dimensional sparse bilinear representation. Based on this representation, a TS-JBE approach was proposed to jointly estimate the cascaded sparse channel gains, VRs, and off-grid parameters. Simulations showed that the proposed approach significantly improves NMSE compared with existing methods.

APPENDIX

A. Proof of Proposition 1

The $(n_x, (n_{\bar{y}} - 1)N + n_y)$ -th element of $\bar{\mathbf{W}} * \mathbf{F}_N^*$, given by $\bar{\mathbf{W}}(n_x, n_{\bar{y}}) \mathbf{F}_N^*(n_x, n_y)$, is expressed as

$$\phi_{n_x, n_{\bar{y}}} e^{-j\frac{2\pi}{\lambda} \left(-(n_x-1)d(\vartheta_{n_{\bar{y}}}-\varphi_{n_y}) + \frac{d^2(n_x-1)^2}{2r_{n_{\bar{y}}}} (1-\vartheta_{n_{\bar{y}}}^2) \right)}, \quad (68)$$

where $n_x, n_y \in \mathcal{N}$ and $n_{\bar{y}} \in \bar{\mathcal{N}}$. Define $\bar{\varphi} = \vartheta_{n_{\bar{y}}} - \varphi_{n_y}$ and $\bar{r} = \frac{r_{n_{\bar{y}}}(1-\varphi^2)}{1-\vartheta_{n_{\bar{y}}}^2}$. Then, (68) can be rewritten as

$$\phi_{n_x, n_{\bar{y}}} e^{-j\frac{2\pi}{\lambda} \left(-(n_x-1)d\bar{\varphi} + \frac{d^2(n_x-1)^2}{2\bar{r}} (1-\bar{\varphi}^2) \right)}. \quad (69)$$

The phase term in (69) matches the analytical form of a near-field ARV, while the amplitude term corresponds to the VR indicator. Consequently, each column of $\bar{\mathbf{W}} * \mathbf{F}_N^*$ can be interpreted as a near-field ARV parameterized by $(\bar{\varphi}, \bar{r})$ and weighted by the associated VR indicator. By constructing a new polar-domain grid $\{(\bar{\varphi}_q, \bar{r}_q)\}_{q=1}^{\bar{Q}}$ over $(\bar{\varphi}, \bar{r})$, where \bar{Q} denotes the number of grid points, the associated ARVs form an equivalent near-field dictionary \mathbf{Q} . Meanwhile, a VR matrix $\bar{\Phi}$ is introduced to maintain a one-to-one correspondence after the dictionary transformation. As a result, $\bar{\mathbf{W}} * \mathbf{F}_N^*$ admits the equivalent representation $\mathbf{Q} \odot \bar{\Phi}$.

REFERENCES

- [1] H. Lu, Y. Zeng, C. You, Y. Han, J. Zhang, Z. Wang, Z. Dong, S. Jin, C.-X. Wang, T. Jiang, X. You, and R. Zhang, "A tutorial on near-field XL-MIMO communications toward 6G," *IEEE Commun. Surveys Tuts.*, vol. 26, no. 4, pp. 2213–2257, 4th Quart. 2024.
- [2] C. You, Y. Cai, Y. Liu, M. Di Renzo, T. M. Duman, A. Yener, and A. Lee Swindlehurst, "Next generation advanced transceiver technologies for 6G and beyond," *IEEE J. Sel. Areas Commun.*, vol. 43, no. 3, pp. 582–627, Mar. 2025.
- [3] X. Shao, C. You, and R. Zhang, "Intelligent reflecting surface aided wireless sensing: Applications and design issues," *IEEE Wireless Commun.*, vol. 31, no. 3, pp. 383–389, Jun. 2024.
- [4] M. Rihan, A. Zappone, S. Buzzi, G. Fodor, and M. Debbah, "Passive versus active reconfigurable intelligent surfaces for integrated sensing and communication: Challenges and opportunities," *IEEE Network*, vol. 38, no. 3, pp. 218–226, May 2024.
- [5] B. Zheng, C. You, W. Mei, and R. Zhang, "A survey on channel estimation and practical passive beamforming design for intelligent reflecting surface aided wireless communications," *IEEE Commun. Surveys Tuts.*, vol. 24, no. 2, pp. 1035–1071, 2nd Quart. 2022.
- [6] D. Mishra and H. Johansson, "Channel estimation and low-complexity beamforming design for passive intelligent surface assisted MISO wireless energy transfer," in *Proc. IEEE Int. Conf. Acoust., Speech Signal Process. (ICASSP)*, May 2019, pp. 4659–4663.
- [7] Y. Wei, M.-M. Zhao, M.-J. Zhao, and Y. Cai, "Channel estimation for IRS-aided multiuser communications with reduced error propagation," *IEEE Trans. Wireless Commun.*, vol. 21, no. 4, pp. 2725–2741, Apr. 2022.
- [8] C. You, B. Zheng, and R. Zhang, "Channel estimation and passive beamforming for intelligent reflecting surface: Discrete phase shift and progressive refinement," *IEEE J. Sel. Areas Commun.*, vol. 38, no. 11, pp. 2604–2620, Nov. 2020.
- [9] Q. Li, M. El-Hajjar, I. Hemadeth, Y. Mestrah, A. Shojaeifard, and L. Hanzo, "Low-complexity channel estimation for RIS-assisted multi-user wireless communications," in *Proc. IEEE Int. Conf. Commun. (ICC)*, Jun. 2025, pp. 6179–6184.
- [10] X. Bian, W. Xu, and Y. Wang, "Sparse representation-based robust channel estimation in XL-RIS-assisted systems," in *Proc. IEEE 100th Vehicular Technology Conference (VTC-Fall)*, Oct. 2024, pp. 1–6.
- [11] M. Gao, H. Li, Y. Wang, and J. Yang, "Sparsity channel estimation for reconfigurable intelligent surface aided MIMO systems," in *Proc. IEEE Int. Symp. Pers., Indoor Mobile Radio Commun. (PIMRC)*, Sep. 2023, pp. 1–6.
- [12] J. Lee and S. Hong, "Near-field LoS/NLoS channel estimation for RIS-aided MU-MIMO systems: Piece-wise low-rank approximation approach," *IEEE Trans. Wireless Commun.*, vol. 24, no. 6, pp. 4781–4792, Jun. 2025.
- [13] Z.-Q. He and X. Yuan, "Cascaded channel estimation for large intelligent metasurface assisted massive MIMO," *IEEE Wireless Commun. Lett.*, vol. 9, no. 2, pp. 210–214, Feb. 2020.
- [14] M. Cui and L. Dai, "Channel estimation for extremely large-scale MIMO: Far-field or near-field?" *IEEE Trans. Commun.*, vol. 70, no. 4, pp. 2663–2677, Apr. 2022.
- [15] S. Yang, W. Lyu, Z. Hu, Z. Zhang, and C. Yuen, "Channel estimation for near-field XL-RIS-aided mmWave hybrid beamforming architectures," *IEEE Trans. Veh. Technol.*, vol. 72, no. 8, pp. 11029–11034, Aug. 2023.
- [16] X. Tuo, Z. Chen, M.-M. Zhao, C. You, and M.-J. Zhao, "Near-field sparse Bayesian channel estimation and tracking for XL-RIS-aided wideband mmWave systems," *arXiv preprint arXiv:2511.18752*, 2025.
- [17] E. Dong, Z. Lian, Y. Wang, Y. Li, Y. Su, B. Wang, and L. Ling, "Double-IRS auxiliary mmWave near-field communications: Channel modeling and performance analysis," *IEEE Internet Things J.*, vol. 12, no. 11, pp. 16023–16036, Jun. 2025.
- [18] E. D. Carvalho, A. Ali, A. Amiri, M. Angelichinoski, and R. W. Heath, "Non-stationarities in extra-large-scale massive MIMO," *IEEE Wireless Commun.*, vol. 27, no. 4, pp. 74–80, Aug. 2020.
- [19] Y. Han, S. Jin, C.-K. Wen, and T. Q. S. Quek, "Localization and channel reconstruction for extra-large RIS-assisted massive MIMO systems," *IEEE J. Sel. Top. Signal Process.*, vol. 16, no. 5, pp. 1011–1025, Aug. 2022.
- [20] X. Yu, W. Shen, R. Zhang, C. Xing, and T. Q. S. Quek, "Channel estimation for XL-RIS-aided millimeter-wave systems," *IEEE Trans. Commun.*, vol. 71, no. 9, pp. 5519–5533, Sep. 2023.
- [21] Z. Yuan, J. Zhang, Y. Ji, G. F. Pedersen, and W. Fan, "Spatial non-stationary near-field channel modeling and validation for massive MIMO systems," *IEEE Trans. Antennas Propag.*, vol. 71, no. 1, pp. 921–933, Jan. 2023.
- [22] K. Liu, Z. Zhang, and L. Dai, "User-side RIS: Realizing large-scale array at user side," in *Proc. IEEE Global Communications Conference (GLOBECOM)*, Dec. 2021, pp. 1–6.
- [23] K. T. Selvan and R. Janaswamy, "Fraunhofer and Fresnel distances: Unified derivation for aperture antennas," *IEEE Antennas Propag. Mag.*, vol. 59, no. 4, pp. 12–15, Aug. 2017.
- [24] C. Zhou, C. You, S. Gong, B. Lyu, B. Zheng, and Y. Gong, "Channel estimation for XL-IRS assisted wireless systems with double-sided visibility regions," in *Proc. IEEE 16th Int. Conf. Wireless Commun. Signal Process. (WCSP)*, Oct. 2024, pp. 456–461.
- [25] A. Tang, J.-B. Wang, Y. Pan, W. Zhang, X. Zhang, Y. Chen, H. Yu, and R. C. de Lamare, "Joint visibility region and channel estimation for extremely large-scale MIMO systems," *IEEE Trans. Commun.*, vol. 72, no. 10, pp. 6087–6101, Oct. 2024.
- [26] X. Zhang, *Matrix analysis and applications*. Cambridge, U.K.: Cambridge Univ. Press, 2017.
- [27] A. Liu, G. Liu, L. Lian, V. K. N. Lau, and M.-J. Zhao, "Robust recovery of structured sparse signals with uncertain sensing matrix: A turbo-VBI approach," *IEEE Trans. Wireless Commun.*, vol. 19, no. 5, pp. 3185–3198, May 2020.
- [28] P. Schniter, "Turbo reconstruction of structured sparse signals," in *Proc. 2010 44th Annu. Conf. Information Sciences and Systems (CISS)*, Mar. 2010, pp. 1–6.
- [29] D. G. Tzikas, A. C. Likas, and N. P. Galatsanos, "The variational approximation for Bayesian inference," *IEEE Signal Process Mag.*, vol. 25, no. 6, pp. 131–146, Nov. 2008.
- [30] W. Xu, A. Liu, B. Zhou, and M.-J. Zhao, "Successive linear approximation VBI for joint sparse signal recovery and dynamic grid parameters estimation," *IEEE Trans. Wireless Commun.*, vol. 24, no. 11, pp. 9645–9659, Nov. 2025.
- [31] A. Liu, Y. Zhou, and W. Xu, "Subspace constrained variational Bayesian inference for structured compressive sensing with a dynamic grid," *IEEE Trans. Signal Process.*, vol. 73, pp. 781–794, Jan. 2025.
- [32] L. Chen, A. Liu, and X. Yuan, "Structured turbo compressed sensing for massive MIMO channel estimation using a Markov prior," *IEEE Trans. Veh. Technol.*, vol. 67, no. 5, pp. 4635–4639, May 2018.
- [33] J. Nocedal and S. J. Wright, *Numerical Optimization*, 2nd ed. New York, NY, USA: Springer, 2006.
- [34] M. R. Akdeniz, Y. Liu, M. K. Samimi, S. Sun, S. Rangan, T. S. Rappaport, and E. Erkip, "Millimeter wave channel modeling and cellular capacity evaluation," *IEEE J. Sel. Areas Commun.*, vol. 32, no. 6, pp. 1164–1179, Jun. 2014.